ISSN 2718-322X (Online)

Engineering Power

BULLETIN OF THE CROATIAN ACADEMY OF ENGINEERING Vol. 20(4) 2025

EDITOR-IN-CHIEF'S WORD

Dear readers,

It is my pleasure to present a new issue of Engineering Power, dedicated to contemporary developments in ship hydrodynamics and marine engineering. The papers published in this issue demonstrate the growing importance of advanced numerical methods, computational modelling, and interdisciplinary research in solving increasingly complex engineering challenges.

Modern marine engineering is undergoing rapid technological transformation driven by high-fidelity simulations, data-driven approaches, and continuous advances in computational science. The contributions collected in this issue reflect both the scientific depth and the practical relevance of these developments, while emphasizing the importance of innovation, reliability, and sustainability in the maritime sector.

I would like to thank all authors for their valuable contributions, as well as the reviewers and editorial team for their dedication and support. Special thanks go to the guest editor, Prof. Nastia Degiuli, PhD, for her excellent work and professional commitment in preparing this issue.

Editor-in-Chief
Vedran Mornar, President of the Croatian Academy of Engineering

EDITOR'S WORD

Dear readers,

I am very pleased to have Prof. Nastia Degiuli, PhD, as the guest editor of the new issue of the Engineering Power journal. Prof. Nastia Degiuli, PhD, is the editor-in-chief of the journal Brodogradnja, which is the highest-ranked journal published in Croatia according to the SCImago Journal Rank. In this issue of Engineering Power, you can read about the numerical determination of the nominal wake of the Japan Bulk Carrier at model scale, propeller open-water characteristics using geometries generated by an automated tool and three-dimensional scanning, high-fidelity propulsion modelling in ship hydrodynamics, meteorological forecast uncertainties in ship speed-loss predictions, and a comprehensive review of non-Newtonian fluid mechanics in engineering and marine applications. I hope you enjoy reading this issue.

Editor
Bruno Zelić, Vice-President of the Croatian Academy of Engineering

FOREWORD

With the rapid development of computational methods, ship hydrodynamics is increasingly driven by high-fidelity numerical simulations supported by validation. While experimental methods remain essential, advanced computational fluid dynamics now enables accurate resolution of complex flow phenomena around hulls and propellers. Key challenges include reliable prediction of the nominal wake, which governs propeller inflow and overall performance, and sensitivity to geometric representation, which can significantly affect open-water characteristics. Coupled simulation frameworks further improve accuracy by capturing hull-propeller interactions under steady and unsteady conditions. In addition, growing attention is given to uncertainty in operational environments, particularly the influence of weather forecast errors on ship speed and performance predictions. Interdisciplinary developments, such as non-Newtonian fluid mechanics, further expand applications in marine engineering. This edition presents five advances in numerical methods and modelling approaches for ship hydrodynamics and marine engineering that contribute to more accurate, reliable, and physically consistent prediction of propulsion performance and operational behaviour.

The first study [1] numerically determines the nominal wake of the Japan Bulk Carrier at model scale using the Reynolds Averaged Navier-Stokes equations with the Shear Stress Transport k-ω turbulence model, validates the results against experimental data, and reports generally good agreement, resulting in an overall deviation of −2.72 %. The second study [2] investigates propeller open-water characteristics using geometries generated by an automated tool and three-dimensional scanning, and demonstrates that the choice of geometric modelling approach significantly affects the predicted thrust, torque, and open water efficiency. The third study [3] presents a high-fidelity sliding mesh approach implemented in OpenFOAM that couples rigid-body motion with propeller rotation, validated against Duisburg Test Case data with accurate prediction of propulsion performance and characteristic frequencies. The fourth study [4] assesses the impact of meteorological forecast uncertainties on ship speed-loss predictions by comparing three computational approaches, and finds that errors in significant wave height have the strongest influence on speed prediction uncertainty, with model-dependent variations in sensitivity across different sea states. The fifth study [5] provides a comprehensive review of non-Newtonian fluid mechanics in engineering and marine applications, highlighting how rheological models and dimensionless analysis support key functions such as drag reduction, flow assurance, and damping.

References

[1] N. Degiuli, C. G. Grlj, I. Martić: A numerical study on the nominal wake of the Japan Bulk Carrier
[2] C. G. Grlj, N. Degiuli, I. Martić, T. Staroveški, L. Berić, I. Heinrich: Comparison of open water characteristics of scanned and generated propellers
[3] I. Sulovsky, Z. Čarija, A. Turk, J. Prpić-Oršić: Insights into high-fidelity propulsion modelling in ship hydrodynamics
[4] M. Marjanović, J. Prpić-Oršić, M. Valčić: Propagation of Weather Forecast Uncertainties through Attainable Ship Speed Prediction Models
[5] M. Bašić, B. Ljubenkov, I. Bezić: Non-Newtonian Fluid Mechanics in Engineering: A Critical Cross-Sector Review from Process Industries to Marine Technology

Guest Editor
Nastia Degiuli, University of Zagreb Faculty of Mechanical Engineering and Naval Architecture

CONTENT

Nastia Degiuli, Carlo Giorgio Grlj, Ivana Martić*

A numerical study on the nominal wake of the Japan Bulk Carrier

University of Zagreb, Faculty of Mechanical Engineering and Naval Architecture, Ivana Lučića 5, Zagreb, 10000, Croatia
*Corresponding author: nastia.degiuli@fsb.unizg.hr

Original scientific paper
Received: November 14, 2025
Accepted: January 9, 2026
https://doi.org/10.65776/ep.20.4.1

Abstract

A key element in propeller design is the accurate determination of the nominal wake. Therefore, in the present study the nominal wake of the Japan Bulk Carrier is determined numerically at model scale, and the numerical results are validated with the available experimental data. The numerical approach is based on the Reynolds Averaged Navier–Stokes (RANS) equations closed with the Shear Stress Transport k-ω (SSTKO) turbulence model. The governing equations are discretized using the Finite Volume Method (FVM) to obtain an algebraic system of equations. The nominal wake is evaluated through numerical simulations that account for the free surface effects. A verification study is performed to quantify the numerical uncertainty associated with the mesh resolution and time step using the Grid Convergence Index (GCI) method. The validation study consists of a comparison between the numerically obtained velocity components and the corresponding experimental measurements. The contour plots of the dimensionless velocity components indicate that the numerically predicted axial velocity is higher than the experimental values, whereas the tangential and radial components show good agreement with the experimental data. The circumferentially averaged dimensionless axial velocity predicted numerically show good agreement between 0.4R to 0.8R, while at radii from 0.8R to 1R, the numerical results overpredict the axial velocity. Finally, the integral values of the nominal wake are calculated, where the relative deviation between the numerical and experimental results is equal to -2.72 %.

Keywords: *CFD, EFD, nominal wake, Japan Bulk Carrier, resistance test*

1. Introduction

The nominal wake, measured at the propeller disc plane, represents one of the most critical aspects of propeller design. Its accurate determination is essential not only for defining the propeller blade section geometry and local pitch distribution but also for evaluating the efficiency of Energy Saving Devices (ESDs) [1]. Traditionally, full-scale nominal wake predictions rely on towing tank measurements conducted at the model scale. However, due to the limited number of validation studies, no firm conclusions can be drawn regarding the accuracy of different wake-scaling procedures. Pronounced scale effects are observed because the nominal wake is strongly influenced by viscous phenomena [2, 3]. These effects manifest as lower axial velocity values at the propeller disc plane in model-scale conditions compared to full scale [4].

Zhang et al. [5] investigated the nominal wake at both model and full scale using numerical simulations in oblique flow and reported a lower mean wake fraction in full-scale simulations. The authors attributed this difference to viscous effects, particularly the relatively thicker boundary layer at model scale. Similarly, Dogrul et al. [6] performed viscous flow simulations around the KCS and KVLCC2 hull forms at different scales and observed reduced axial velocities obtained for lower Reynolds numbers, further confirming the significant scale dependency of the nominal wake.

Conventionally, towing tank experiments are employed to determine the nominal wake at model scale. Since such measurements in the towing tank are expensive and time-consuming, Computational Fluid Dynamics (CFD) has become an attractive alternative for both model- and full-scale analyses. As demonstrated by Farkas et al. [4], performing full-scale CFD simulations eliminates the need for wake-scaling corrections prescribed by the International Towing Tank Conference (ITTC) and avoids the associated uncertainties. The authors emphasized that full-scale CFD simulations offer distinct advantages for stern-flow optimization and the validation of ESD performance.

The influence of surface conditions on propeller performance and wake characteristics has also been highlighted in recent studies. Farkas et al. [7] performed numerical simulations of the open water test to evaluate the effect of biofouling on propeller open water characteristics. The study led to a new performance prediction method for fouled surfaces. The authors pointed out that additional investigations are required to assess the influence of surface roughness and fouling on propellers operating in a ship's wake. Subsequently, Farkas et al. [8] investigated the influence of biofilm on the nominal wake and demonstrated that its presence can reduce the integral value of the nominal wake of a bulk carrier by up to 7 %.

Wang et al. [9] examined the influence of scale effects on the nominal wake of a 4000 TEU containership through CFD simulations. The authors compared Double Body Simulations (DBS), which neglect the free surface effects, with Free Surface Simulations (FSS) and found that the free surface has a negligible influence on the nominal wake. However, a distinct dependence of the mean axial wake fraction on the Reynolds number was observed, which prompted the authors to propose a new scaling method. Guo et al. [10] further examined the nominal wake for the case of the KCS by modifying the aft hull form to reproduce a full-scale like wake distribution. Their results, validated using particle image velocimetry, demonstrated that the modified hull configuration effectively minimized scale-induced discrepancies, and the authors proposed a new approach to mitigate scale effects in nominal wake prediction.

The aim of the present study is the numerical determination of the nominal wake of the Japan Bulk Carrier (JBC) and the validation of the obtained results with the available experimental data [11]. The FSS where conducted to include the effects of the free surface on the numerically obtained nominal wake. The rest of the paper is structured as follows: Section 2 describes the case study, outlines the mathematical background of the numerical simulations, and presents the experimental setup. Section 3 discusses the results of the verification and validation studies. Finally, Section 4 summarizes the main conclusions and outlines directions for future work.

2. Methods

2.1 Case study

The JBC is used as a case study in the numerical analysis of the nominal wake. The JBC is a capsize bulk carrier that has a bulbous bow and a transom stern. It was developed by the National Maritime Research Institute at the Yokohama National University and the Ship Building Research Centre of Japan for the purposes of the CFD workshop held in 2015 [12]. In Table 1, the main parameters can be seen, and the 3D model is shown in Figure 1. Figure 2 illustrates the location of the propeller plane, along with the global coordinate system. The coordinate system is defined with its origin at the intersection of the aft perpendicular and the waterplane. The x-axis points toward the bow, the z-axis is oriented upward, and the y-axis is directed toward the port side.

Main Parameter	Value
Scale λ	40.264
Length between perpendiculars L_{PP}, m	6.954
Length of waterline L_{WL}, m	7.078
Breadth B, m	1.118
Draught T, m	0.410
Displacement volume ∇, m^3	2.733

Table 1. JBC main parameters.

Fig. 1. Isometric and side views of the 3D model used in the numerical simulations.

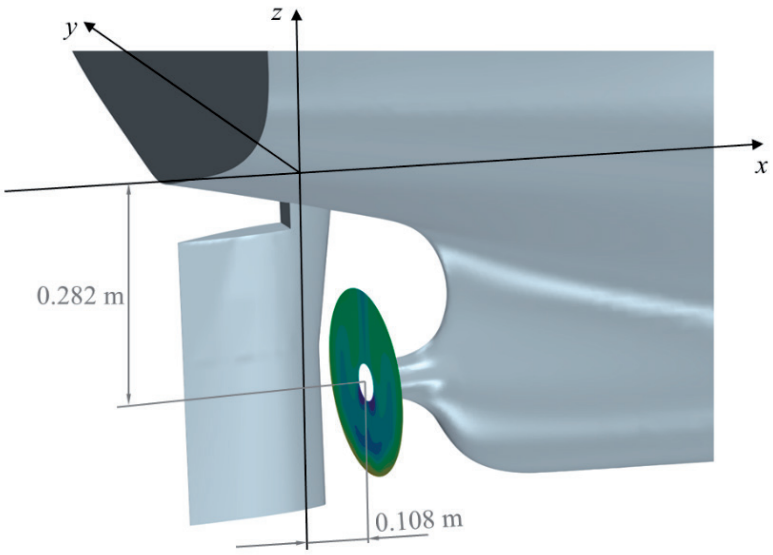

Fig. 2. Position of the propeller disc and the global coordinate system.

2.2 Experimental setup

The scale was selected to match the one used in the towing tank tests conducted at the Brodarski Institute in Zagreb [13]. As a part of the Croatian Science Foundation research project "Sustainable slow steaming for low carbon shipping", STARSHIP, an extensive experimental campaign was conducted including the resistance, open water and self-propulsion tests. The experimental campaign also included the measurements of the nominal wake. The nominal wake was obtained by measuring the absolute and static pressure using a five-hole Prandtl Pitot tube [11]. Figure 3 shows the installed five-hole Prandtl Pitot tube in the stern region, near the propeller.

Fig. 3. The five-hole Prandtl Pitot tube installed at the stern.

By subtracting the measured pressure values, the velocity components were calculated. The velocity components were obtained at radial positions equal to 0.35*R*, 0.55*R*, 0.74*R*, 0.94*R*, and 1.04*R* and at angular positions from 0° to 360° with 10° increments. According to long-term practice at the Brodarski Institute, the uncertainty associated with the measurements of absolute and static pressures at the propeller plane is within ±3 % [14].

2.3 Mathematical formulation

The numerical simulations are conducted with the commercial software STAR-CCM+ version 2306 [15] in which the mathematical model is based on Reynolds averaged Navier-Stokes (RANS) equations which read as follows:

$$\frac{\partial \overline{u}_i}{\partial x_i} = 0 \tag{1}$$

$$\rho \frac{\partial \overline{u}_i}{\partial t} + \rho \frac{\partial}{\partial x_j}(\overline{u}_i \overline{u}_j + \overline{u_i' u_j'}) = -\frac{\partial \overline{p}}{\partial x_i} + \frac{\overline{\tau}_{ij}}{\partial x_j} \tag{2}$$

where ρ is the fluid density, $\overline{u}_i$ is the averaged Cartesian component of the velocity vector, $\rho \overline{u_i' u_j'}$ is the Reynolds Stress Tensor (RST), $\overline{p}$ is the mean pressure, and $\overline{\tau}_{ij}$ is the mean viscous stress tensor.

For the closure of the governing equations, the two-equation Shear Stress Transport *k-ω* (SSTKO) turbulence model was used [14]. Within the SSTKO turbulence model two additional equations, one for the turbulent kinetic energy *k* and one for the specific dissipation *ω* are solved:

$$\frac{\partial}{\partial t}(\rho k) + \frac{\partial}{\partial x_i}(\rho k \overline{u}_i) = \frac{\partial^2 k}{\partial x_i^2}(\mu + \sigma_k \mu_t) + G_k + G_{nl} + \\ + G_b - \rho \beta^* f_{\beta^*}(\omega k - \omega_0 k_0) + S_k \tag{3}$$

$$\frac{\partial}{\partial t}(\rho \omega) + \frac{\partial}{\partial x_i}(\rho \omega \overline{u}_i) = \frac{\partial^2 \omega}{\partial x_i^2}(\mu + \sigma_\omega \mu_t) + G_\omega + D_\omega - \\ - \rho \beta f_\beta(\omega^2 - \omega_0{}^2) + S_\omega \tag{4}$$

where μ is the dynamic viscosity coefficient of the fluid, μ_t is the turbulent eddy viscosity, σ_k, σ_ω, β, and β^* are model coefficients, G_k, G_{nl}, G_b, and G_ω are the turbulent, non-linear, buoyancy, and specific dissipation production terms, respectively, f_{β^*} is the vortex-stretching modification factor, f_β is the free-shear modification factor, k_0 and ω_0 are the ambient values that counteract turbulence decay, and finally, S_k and S_ω are the user-specified source terms.

The governing differential equations were discretized using the Finite Volume Method (FVM). Since the numerical simulations accounted for the presence of a free surface, the interaction between the two immiscible fluids, i.e., water and air, was modelled using the Volume of Fluid (VOF) method. To ensure accurate resolution of the interface between the two phases, the High-Resolution Interface Capturing (HRIC) scheme was employed. Also, gravity is considered in the numerical simulations.

2.4 Numerical setup

In the present study, the numerical simulations that include the free surface effects are conducted, i.e., FSS. The numerical simulations are conducted at model scale to be able to validate the obtained results by directly comparing them to the experimental measurements. The computational domain in the FSS is generated according to the ITTC recommendations [16, 17]. In Figure 4 details of the computational domain are shown. The computational boundaries are placed at a distance large enough to prevent any undesired influence on the numerical solution. Velocity inlet is applied at the inlet, top and bottom boundaries, while outlet pressure is defined at the outlet boundary. At the side boundaries the symmetry boundary condition is used. For the hull and rudder surfaces, the no-slip wall boundary condition is applied. To avoid the wave reflections from the domain boundaries, the wave damping method [18] is applied at the inlet, outlet and side boundaries.

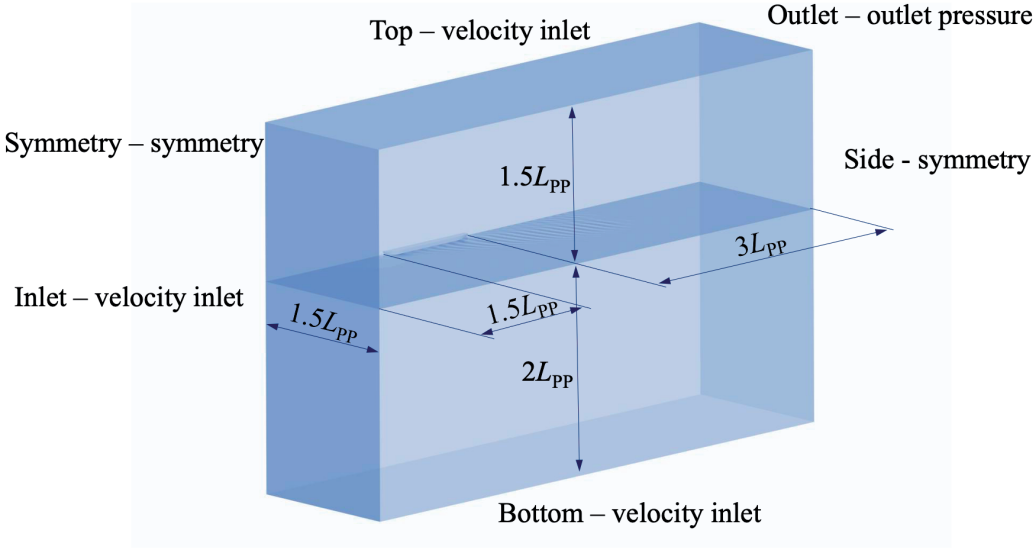

Fig. 4. Details of the computational domain.

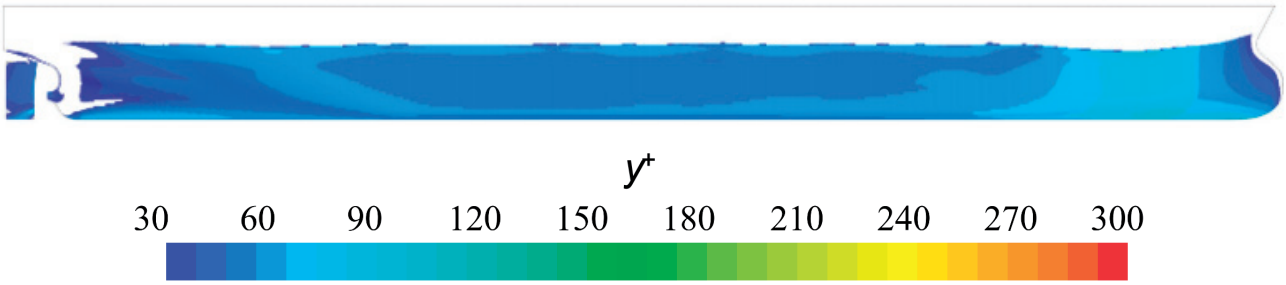

Fig. 5. Dimensionless wall distance y^+ obtained on the hull and rudder surfaces of the JBC.

The computational domain is discretized using unstructured hexahedral cells. The mesh is further refined in the following regions: free surface, Kelvin wake, bow, stern, and around the propeller disc.

The boundary layer is solved by applying wall functions and thus, the dimensionless wall distance y^+ is maintained above 30, as shown in Figure 5. The SSTKO turbulence model combined with wall functions was selected as a compromise between the computational resources needed to conduct the numerical simulations and the accuracy of the numerical results.

To maintain the y^+ value above 30, prism layers are generated in the vicinity of the hull and rudder surfaces. The distance between the centre of the first cell near the wall and the wall is carefully selected and additional prism layers are generated to keep a smooth transition to the rest of the mesh. Detailed views of the generated mesh with all applied refinements are presented in Figures 6 and 7.

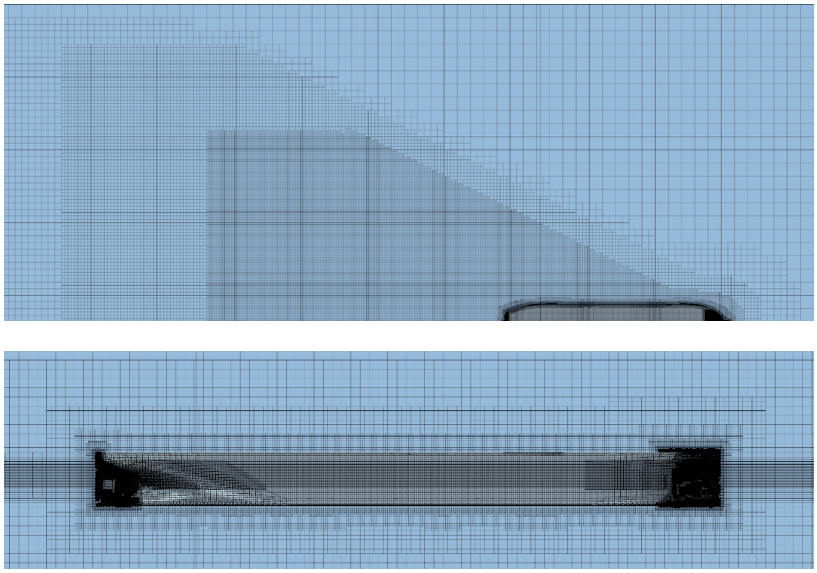

Fig. 6. The top and side views of the generated mesh.

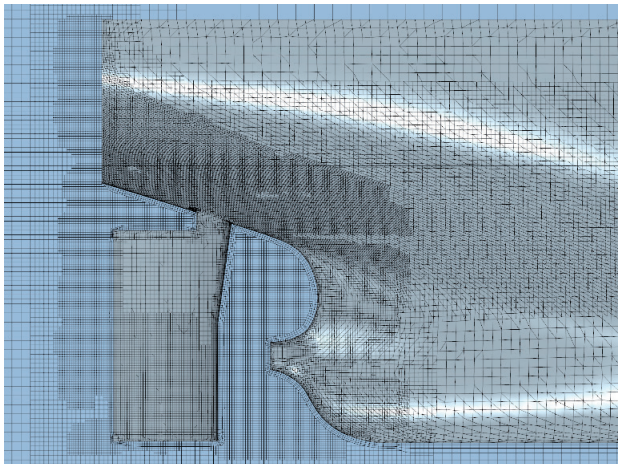

Fig. 7. Mesh details at the stern, near the propeller plane.

The numerical schemes used to solve the temporal, convection and gradient terms are selected following the recommendations given by Grlj et al. [19]. First-order discretization scheme is used for the temporal discretization, while second-order schemes are used for solving the convection and gradient terms.

The numerical simulations are carried out assuming smooth surfaces for both the hull and the rudder, and a fully developed turbulent flow throughout the computational domain. A freshwater density of 999.49 kg/m³ is used to replicate the conditions of the towing tank experiments, while the dynamic viscosity is set to 0.0012584 Pa·s. Since the towing tank measurements are performed at the design speed of the JBC, the inflow velocity in the numerical simulations is set to 1.176 m/s, which corresponds to a full-scale speed of 14.5 knots.

3. Results

3.1 Verification study

A verification study is conducted to assess the numerical uncertainty due to mesh resolution and time step. For the verification study, the Grid Convergence Index (GCI) method is used [20-22]. Three meshes are generated for the verification study, Table 2. The fine time step is defined as 0.125 % L_{PP}/v, while the medium and coarse time steps are obtained by multiplying the fine time step by 2 and 4, respectively.

Mesh	Number of cells N	Grid spacing h, m	Time step, s
Fine	3.5M	0.162	0.0074
Medium	1.7M	0.204	0.0148
Coarse	0.6M	0.282	0.0296

Table 2. Mesh sizes and time steps used in the verification study.

The verification study is conducted for the integral value of the nominal wake w_n. Table 3 shows the obtained results. The reported numerical uncertainty due to the mesh resolution is above 8 %. The reported order of method is close to 2, which indicates that the calculated *GCI* is reliable. The high numerical uncertainty can be attributed to the geometry of the JBC, which has a large block coefficient and exhibits strong flow recirculation in the stern region. Thus, the velocity distribution in the stern region varies a lot and to capture the local flow phenomenon fully, a more robust approach should be considered.

In contrast to the verification study for mesh resolution, the time step verification yielded better results, with the predicted *GCI* equal to 0.42 %. The observed order of method p, was considerably lower than the theoretical value of 2, indicating an overestimation of the computed numerical uncertainty. Consequently, the uncertainty associated with the time step can be considered negligible compared to that arising from the mesh resolution.

Parameter	Mesh resolution	Time step
ε_{21}	0.039	-0.002
ε_{32}	0.040	0.003
R	0.975	-0.570
p	2.196	0.820
ϕ_{ext}^{21}	0.600	0.646
e_{a}^{21}	0.061	0.003
e_{ext}^{21}	0.076	0.003
GCI_{fine}^{21}	8.83 %	0.42 %

Table 3. The verification study results.

3.2 Validation study

The numerical results presented in this subsection were obtained using the fine mesh and time step after the velocity components at the propeller plane had converged. The results presented in this subsection correspond to the final time step. Since the experimental velocity data below 0.4R were extrapolated, only values for higher radii are shown.

Figure 8 shows the comparison between the numerically and experimentally obtained distributions of the dimensionless axial velocity component at the propeller disc. The dimensionless axial velocity component predicted numerically is higher than the experimental values. A reason for this is the presence of rudder in the numerical simulations as opposed to the experimental setup. This is because the Prandtl Pitot tube was used in the towing tank and the installation of the required equipment occupied the stern area, specifically the rudder region. The hook like shape is visible in both cases, but the speed reductions obtained in the towing tank are greater compared to the speed reduction obtained numerically. In the region closer to the hub, the speed reductions predicted numerically are greater than those obtained experimentally.

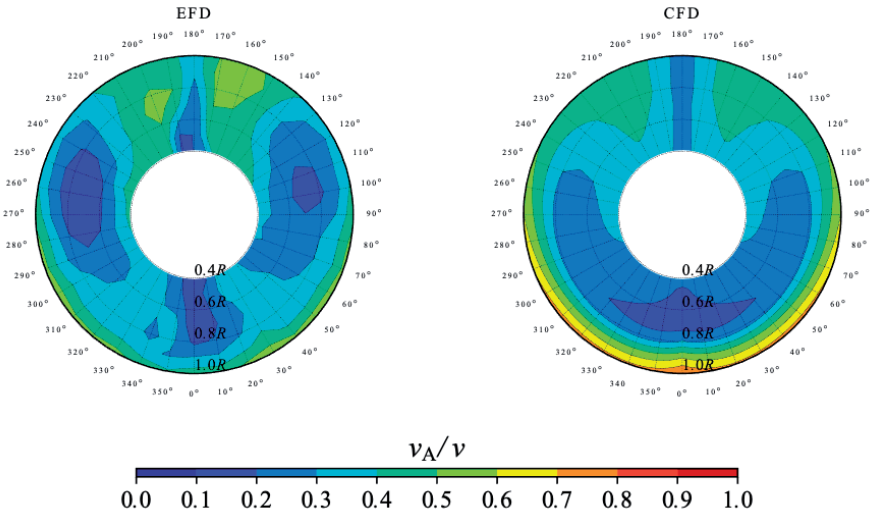

Fig. 8. Comparison between the numerical and experimental results of the dimensionless axial velocity component at the propeller disc.

A more detailed representation of the axial velocity component is shown in Figure 9, where the circumferential distributions of the dimensionless axial velocity for radii ranging from 0.4R to 1R are presented. The numerically predicted axial velocity between 0.4R and 0.8R show good agreement with the experimental data. At radii from 0.8R to 1R, however, the numerically obtained axial velocity becomes higher than the experimental values. There are larger speed reductions at circumferential position from 80° to 140° and likewise from 220° to 290° at radii from 0.6R to 0.8R. Also, at radii 0.6R and 0.7R larger discrepancies are evident from 0° to 60° and from 300° to 360°.

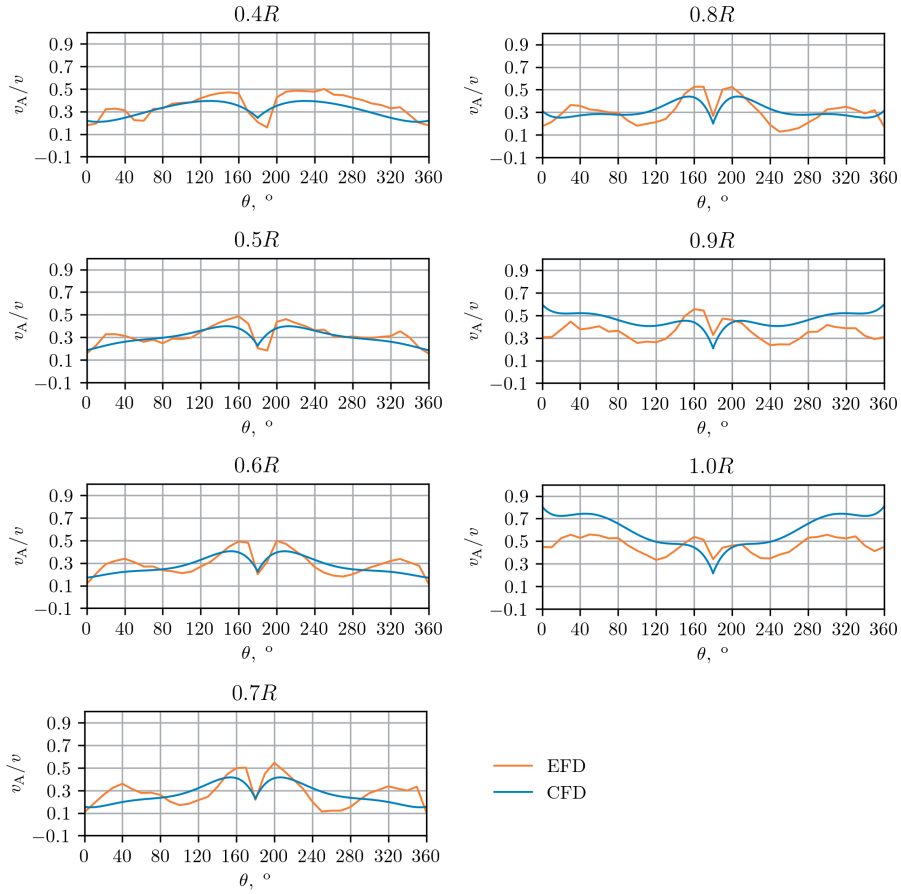

Fig. 9. The numerically and experimentally obtained circumferential distributions of the dimensionless axial velocity component at radii from 0.4R to 1R.

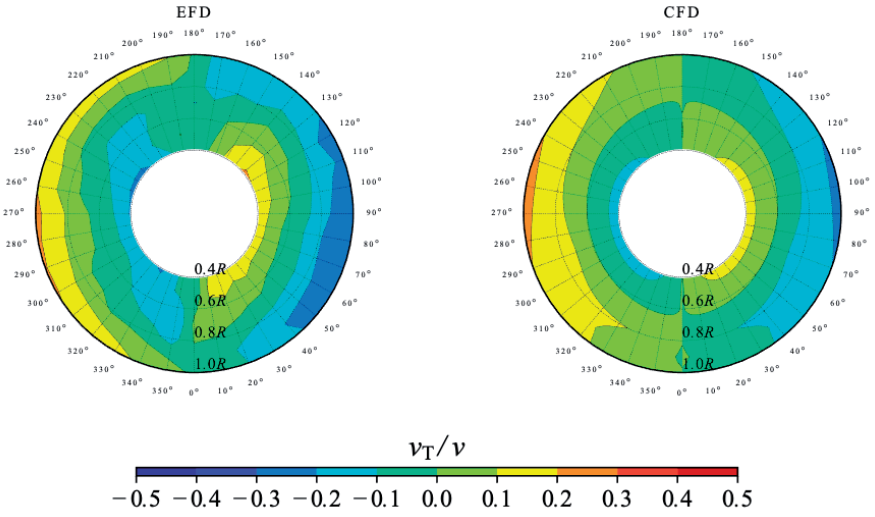

Fig. 10. Comparison between the numerical and experimental results of the dimensionless tangential velocity component at the propeller disc.

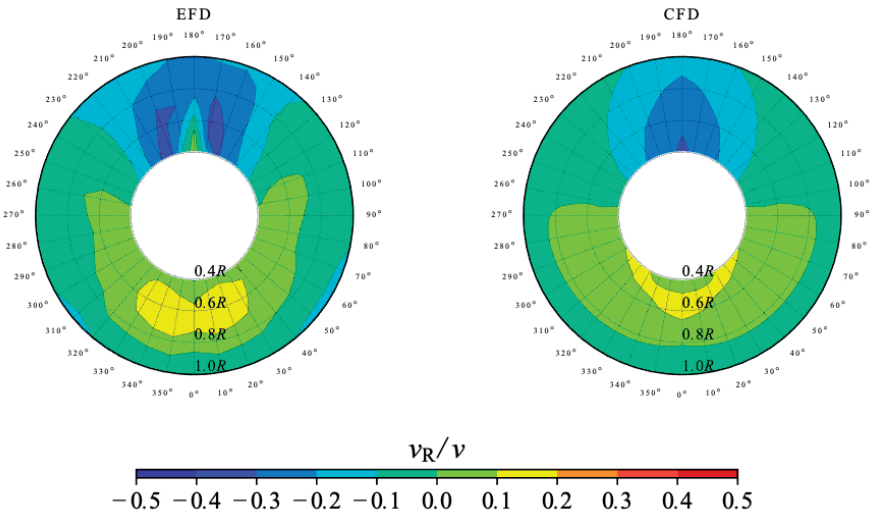

Fig. 11. Comparison between the numerical and experimental results of the dimensionless radial velocity component at the propeller disc.

Figures 10 and 11 show the comparisons of the tangential and radial velocity components obtained numerically and experimentally, respectively. Overall, the numerically predicted flow patterns agree well with the experimental observations. However, the experimental results exhibit a higher tangential velocity component in the region closer to the propeller hub compared to the numerical predictions. Similarly, in the region near the propeller tip, the tangential velocity measured in the towing tank is greater than that obtained from the numerical simulations. The towing tank measurements reveal an increase in the radial velocity component above the propeller hub that is not captured in the numerical simulations. Moreover, the experimental results show a more pronounced variation in the magnitude of the radial velocity component both above and below the hub compared to the numerical predictions.

Figure 12 presents the radial distribution of the circumferentially averaged dimensionless axial velocity component comparing the numerical and experimental results. Noticeable differences are observed between the numerical and experimental results in the range from 0.4R to 0.8R, while the discrepancies decrease with increasing radial position. At smaller radii, the numerically obtained axial velocity is lower than the experimental values, whereas between 0.9R and 1R it becomes slightly higher.

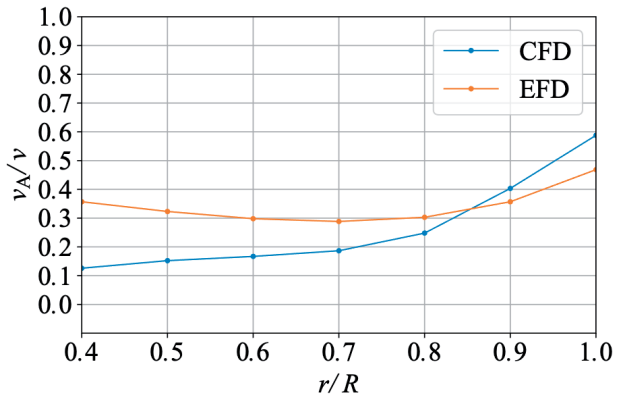

Fig. 12. Radial distribution of the circumferentially averaged dimensionless axial velocity component.

Finally, the integral value of the nominal wake is calculated as:

$$w_n = 1 - \frac{v_A}{v} \tag{5}$$

where v is the ship speed and v_A is the averaged axial velocity component over the propeller disc.

The numerically obtained integral value of the nominal wake is equal to 0.640, while the value derived from the experimental data is equal to 0.658. This corresponds to a relative deviation of only -2.72 %, indicating that despite local discrepancies in the axial velocity distribution, the overall nominal wake can be accurately predicted by the numerical simulations at model scale.

4. Conclusions

Numerical simulations of the resistance test were performed for the Japan Bulk Carrier at model scale, with particular emphasis on the flow characteristics in the propeller disc region. The presented results include contours of the dimensionless velocity components, axial, tangential, and radial, as well as the radial and circumferential distributions of the dimensionless axial velocity and the integral value of the nominal wake. A comprehensive verification study was carried out to quantify the numerical uncertainty associated with mesh resolution and time step. The findings revealed that mesh resolution had a major impact on the numerical uncertainty, while the influence of the time step was comparatively smaller. This can be attributed to the presence of recirculation zones in the stern region of the Japan Bulk Carrier, which caused fluctuations in the computed integral value of the nominal wake.

The validation study, based on the comparison of numerical and experimental results, showed that the numerically predicted dimensionless axial velocity component was generally higher than the experimental measurements, although the

characteristic hook like pattern was accurately reproduced. The contours of the tangential and radial velocity components also exhibited good agreement with the experimental data. The numerically obtained radial distribution of the circumferentially averaged axial velocity was lower than the experimental values between 0.4*R* and 0.8*R* but exceeded them at higher radii. Despite these local discrepancies, the relative deviation between the numerically and experimentally obtained integral values of the nominal wake was only -2.72 %, demonstrating that the overall wake characteristics were well captured by the numerical model.

5. Acknowledgement

This work was supported by the Croatian Science Foundation under the project number IP-2025-02-4779.

6. References

[1] Park, S., Oh, G., Rhee, S. H., Koo, B. Y., Lee, H. Full scale wake prediction of an energy saving device by using computational fluid dynamics. Ocean Eng. 101 (2015) 254-263.

[2] Regener, P., Mirsadraee, Y., Andersen, P. Nominal vs. effective wake fields and their influence on propeller cavitation performance. J. Mar. Sci. Technol. 6(2) (2018) 34.

[3] Ma, Z., Ji, N., Zeng, Q., Deng, X. and Shi, C. Influence of scale effect on flow field offset for ships in confined waters. Brodogradnja 75(1) (2024), 75106.

[4] Farkas, A., Degiuli, N., Martić, I., Dejhalla, R. Numerical and experimental assessment of nominal wake for a bulk carrier. J. Mar. Sci. Technol. 24 (2019), 1092-1104.

[5] Zhang, Y. X., Lai, M. Y., Ni, Y. G., Feng, L. CFD study of hull wakes in oblique flow at model and full scales. Appl. Ocean Res. 112 (2021) 102689.

[6] Dogrul, A., Song, S., Demirel, Y. K. Scale effect on ship resistance components and form factor. Ocean Eng. 209 (2020) 107428.

[7] Farkas, A., Degiuli, N., Martić, I. The impact of biofouling on the propeller performance. Ocean Eng. 219 (2021) 108376.

[8] Farkas, A., Degiuli, N., Martić, I. Impact of biofilm on the resistance characteristics and nominal wake. Proc. Inst. Mech. Eng. M: J. Eng. Marit. Environ. 234 (2020) 59-75.

[9] Wang, Z. Z., Xiong, Y., Wang, R., Shen, X. R., Zhong, C. H. Numerical study on scale effect of nominal wake of single screw ship. Ocean Eng. 104 (2015) 437-451.

[10] Guo, C., Wu, T., Zhang, Q., Luo, W., Su, Y. Numerical simulation and experimental studies on aft hull local parameterized non-GEOSIM deformation for correcting scale effects of nominal wake field. Brodogradnja 68(1) (2017) 77-96.

[11] Grlj, C.G., Degiuli, N., Martić, I. Scale effects on the resistance and propulsion characteristics of the Japan Bulk Carrier. Ocean Eng. 339 (2025), 122059.

[12] NMRI, 2015. Tokyo 2015 a workshop on CFD in ship hydrodynamics. https://t2015.nmri. go.jp/index.html

[13] Brodarski Institute. Report 6652-M. resistance, self-propulsion and 3D wake measurement test results Project: Japan Bulk Carrier - JBC. Brodarski Institute (2022).

[14] Grlj, C.G., Degiuli, N. and Martić, I. Experimental and numerical assessment of the effect of speed and loading conditions on the nominal wake of a containership. Brodogradnja 75(4) (2024), 75405.

[15] Siemens. STAR-CCM+ User Guide (2020).

[16] ITTC. Practical guidelines for RANS calculation of nominal wakes ITTC (2017).

[17] ITTC. Practical guidelines for ship CFD applications, 7.5-03-02-03. ITTC-Recommended Procedures and Guidelines (2011).

[18] Choi, J., Yoon, S. B. Numerical simulations using momentum source wave-maker applied to RANS equation model. Coast. Eng., 56 (2009) 1043-1060.

[19] Grlj, C. G., Degiuli, N., Martić, I. The impact of numerical parameters on the resistance characteristics of a container ship at the model and full scale. J. Mar. Sci. Eng. 11(9) (2023) 1672.

[20] Celik, I. B., Ghia, U., Roache, P. J., Freitas, C. J., Coleman, H., Raad, P.E. Procedure for estimation and reporting of uncertainty due to discretization in CFD applications. J. Fluids Eng. Trans. ASME. 130 (2008) 078001.

[21] Eça, L., Hoekstra, M. A procedure for the estimation of the numerical uncertainty of CFD calculations based on grid refinement studies. J. Comput. Phys. 262 (2014) 104-130.

[22] Mikulec, M., Piehl, H. Verification and validation of CFD simulations with full-scale ship speed/power trial data. Brodogradnja 74(1) (2023) 41-62.

Carlo Giorgio Grlj, Nastia Degiuli, Ivana Martić, Tomislav Staroveški, Luka Berić, Ivan Heinrich*

Comparison of open water characteristics of scanned and generated propeller

University of Zagreb, Faculty of Mechanical Engineering and Naval Architecture, Ivana Lučića 5, Zagreb, 10000, Croatia
*Corresponding author: nastia.degiuli@fsb.unizg.hr

Original scientific paper
Received: January 15, 2026
Accepted: March 24, 2026
https://doi.org/10.65776/ep.20.4.2

Abstract

This study presents a numerical investigation of open water characteristics using propeller geometry obtained through different approaches: automated approach with an online generator and three-dimensional scanning. The main objective is to evaluate the influence of the chosen geometric modelling approach on the predicted propeller open water characteristics. The turbulent flow around the propeller is modelled using the steady incompressible Reynolds Averaged Navier-Stokes equations and Shear Stress Transport k-ω turbulence model in combination with the γ-$Re_{\theta t}$ transition model, enabling the simulation of both laminar and turbulent flow. Numerical simulations are performed using the commercial Computational Fluid Dynamics software STAR-CCM+ 2310. The methodology follows the recommendations of the International Towing Tank Conference, and verification of the numerical results is carried out through grid independence studies. Validation of the numerical results is performed by comparison with experimental open water data obtained at the Brodarski Institute in Zagreb. The open water characteristics predicted using the scanned and generated propeller are compared in terms of thrust, torque, and open water efficiency. The results provide insight into the sensitivity of propeller performance to geometric modelling approach and highlight the importance of accurate geometry representation in numerical analyses.

Keywords: *CFD, EFD, open water test, containership, Wageningen-B series*

1. Introduction

Computational Fluid Dynamics (CFD) is widely applied in marine engineering for the analysis of the hydrodynamic characteristics of marine propellers. This approach enables detailed investigation of the flow around a propeller without the need for costly and time-consuming towing tank tests. Recent studies have shown that CFD simulations can be used for accurate prediction of the Propeller Open Water (POW) characteristics.

In numerical simulations based on the Reynolds Averaged Navier-Stokes (RANS) equations, various approaches can be employed to simulate propeller operation, such as the overset mesh method [1, 2] or a steady-state approach based on a rotating coordinate system, commonly referred to as the Moving Reference Frame (MRF) method [3-6]. Numerical simulations allow researchers to study the hydrodynamic characteristics of propellers in open water conditions at different scales, thereby enabling investigation of scale effects on propeller performance. Chen et al. [1] investigated the scale effects on the highly skewed INSEAN E1619 propeller and observed a significant effect on the torque coefficient, as well as on pressure and velocity distributions, while the effect on the thrust coefficient was less pronounced. Specifically, at larger scales, higher non-dimensional pressure values were obtained on the suction side, whereas the opposite trend was observed on the pressure side. Dong et al. [4] studied the scale effects on the open water efficiency of the International Towing Tank Conference (ITTC) PPTC-II propeller. The authors observed influence of scale on the thrust coefficient and attributed it to the reduction of boundary-layer thickness on the propeller blades at full scale compared to model scale. Grlj et al. [6] investigated the scale effects on POW characteristics and demonstrated that they can be significantly reduced by applying a transition model. Emphasis was placed on the application of transition model at model scale, which enables improved prediction of laminar and turbulent flow near the propeller blades, thereby reducing discrepancies in the prediction of open water efficiency. The obtained results highlight the importance of careful selection of turbulence models to achieve high simulation accuracy. Studies addressing the application of transition models, particularly the $\gamma - \overline{Re}_{\theta t}$ transition model, indicate that this model improves the prediction of POW characteristics at model scale [7, 8]. By accounting for both laminar and turbulent flow, better agreement between the numerically obtained boundary-layer flow characteristics and experimental data has been achieved for both conventional and highly skewed propellers [9, 10]. Pawar and Brizzolara [11] showed that inclusion of a transition model at model scale improved agreement between numerical and experimental results for both conventional and ducted propellers. Lopes et al. [12] demonstrated that omission of additional terms describing crossflow leads to almost completely laminar flow around the propeller blades. When these terms are included, a significant portion of the flow becomes turbulent, resulting in reduced thrust and torque coefficients.

To obtain the 3D model of the propeller for use in the numerical simulations, different methods can be employed. It can be generated using automated tools such as the online generator for the Wageningen B-series propellers [13]. Another approach for obtaining the 3D model of a

propeller is reverse engineering if the physical propeller model is available. Guan and Gu [14] reconstructed the geometry of a propeller and a ship hull using point cloud data obtained from laser scanning of the surfaces. Njaastad et al. [15] automated the operation of an industrial robot to scan full-scale propeller blades using a high-precision camera and a laser sensor. The authors demonstrated that accurate propeller blade models can be obtained through automated scanning methods. In a more recent study, Njaastad et al. [16] presented a procedure for extracting various geometric parameters of propeller blades using point cloud data as input. The proposed method was validated by determining the propeller parameters for the KVLCC2 ship. Similarly, Zheng et al. [17] proposed a method for reconstructing propeller geometry from point cloud data.

In this study, CFD simulations are used to determine the hydrodynamic characteristics in open water of a Fixed Pitch Propeller (FPP). Numerical predictions of the POW characteristics obtained using a generated propeller geometry are compared with those obtained using a scanned propeller geometry. The remainder of the paper is organized as follows. Section 2 describes the case study, the experimental setup, the mathematical and numerical setup, and two approaches used to obtain the propeller geometry. Section 3 presents the numerical results, while Section 4 summarizes the main findings of the study.

2. Methods

2.1 Case study

The considered propeller is a FPP used for a post-Panamax 6750 TEU containership with the main parameters shown in Table 1.

Main Parameter	Value
Scale λ	35.18
Diameter, D	0.2075 m
Number of blades, Z	4
Expanded area ratio, A_E/A_0	0.75
Pitch ratio, P/D	0.8901
Hub ratio, d/D	0.1687
Rate of revolution, n	25.01 rps
Direction of rotation	Clockwise

Table 1. Propeller main parameters.

The 3D model of the propeller is obtained using two methods, which are explained in the subsection 2.5 in detail.

2.2 Experimental setup

The Open Water Tests (OWT) were conducted at the Brodarski Institute within the Croatian Science Foundation research project "Sustainable slow steaming for low-carbon shipping" [18]. The experimental results are taken from Degiuli et al. [19], where the authors provide a detailed description of the conducted OWT along with a comprehensive analysis of the associated experimental uncertainties. The OWT were conducted for advance coefficients J ranging from 0 to 1 by maintaining a constant rate of revolution and varying the advance speed v_A.

2.3 Mathematical formulation

The numerical simulations of the OWT are based on the RANS equations which read as follows:

$$\frac{\partial \overline{u}_i}{\partial x_i} = 0 \tag{1}$$

$$\rho \frac{\partial \overline{u}_i}{\partial t} + \rho \frac{\partial}{\partial x_j}(\overline{u}_i \overline{u}_j + \overline{u_i' u_j'}) = -\frac{\partial \overline{p}}{\partial x_i} + \frac{\overline{\tau}_{ij}}{\partial x_j} \tag{2}$$

where ρ is the fluid density, $\overline{u}_i$ is the averaged Cartesian component of the velocity vector, $\rho \overline{u_i' u_j'}$ is the Reynolds Stress Tensor (RST), $\overline{p}$ is the mean pressure, and $\overline{\tau}_{ij}$ is the mean viscous stress tensor.

The Shear Stress Transport k-ω (SSTKO) turbulence model is used for the closure of the governing equations. Two additional transport equations are solved: one for the turbulent kinetic energy k and one for the specific dissipation ω:

$$\frac{\partial}{\partial t}(\rho k) + \frac{\partial}{\partial x_i}(\rho k \overline{u}_i) = \frac{\partial^2 k}{\partial x_i^2}(\mu + \sigma_k \mu_t) + G_k + G_{nl} + \\ + G_b - \rho \beta^* f_{\beta^*}(\omega k - \omega_0 k_0) + S_k \tag{3}$$

$$\frac{\partial}{\partial t}(\rho \omega) + \frac{\partial}{\partial x_i}(\rho \omega \overline{u}_i) = \frac{\partial^2 \omega}{\partial x_i^2}(\mu + \sigma_\omega \mu_t) + G_\omega + D_\omega - \\ - \rho \beta f_\beta(\omega^2 - \omega_0^2) + S_\omega \tag{4}$$

where μ is the dynamic viscosity coefficient of the fluid, μ_t is the turbulent eddy viscosity, σ_k, σ_ω, β, and β^* are model coefficients, G_k, G_{nl}, G_b, and G_ω are the turbulent, non-linear, buoyancy, and specific dissipation production terms, respectively, f_{β^*} is the vortex-stretching modification factor, f_β is the free-shear modification factor, k_0 and ω_0 are the ambient values that counteract turbulence decay, and finally, S_k and S_ω are the user-specified source terms.

Since the numerical simulations are conducted at model scale, laminar flow is considered by implementing the $\gamma - \overline{Re}_{\theta t}$ transition model [6]. It consists of solving the transport equations for intermittency γ and transition momentum thickness Reynolds number $\overline{Re}_{\theta t}$, which read as follows:

$$\frac{\partial(\rho\gamma)}{\partial t}+\frac{\partial\left(\rho\overline{u}_j\gamma\right)}{\partial x_j}=P_\gamma-E_\gamma+\frac{\partial}{\partial x_j}\left[\left(\mu+\frac{\mu_t}{\sigma_f}\right)\frac{\partial\gamma}{\partial x_j}\right] \tag{5}$$

$$\frac{\partial\left(\rho\overline{Re}_{\theta t}\right)}{\partial t}+\frac{\partial\left(\rho\overline{u}_j\overline{Re}_{\theta t}\right)}{\partial x_j}=P_{\theta t}+ +\frac{\partial}{\partial x_j}\left[\sigma_{\theta t}\left(\mu+\mu_t\right)\frac{\partial\overline{Re}_{\theta t}}{\partial x_j}\right] \tag{6}$$

where P_γ and $P_{\theta t}$ are production terms, σ_f and $\sigma_{\theta t}$ are model coefficients, and E_γ is the destruction term.

The system of algebraic equations is obtained by discretizing the governing equations with the finite volume method. The rotation of the propeller is accounted for with the steady-state MRF method in which the region around the propeller is defined in a rotating coordinate system. The numerical simulations are performed until the thrust and torque converged for each *J*.

2.4 Numerical setup

The computational domain is cylinder shaped with the dimensions defined according to the ITTC recommendations [20]. The inlet boundary is positioned at 4*D* in front of the propeller and a uniform velocity inlet is defined as the boundary condition. The outlet boundary is set as pressure outlet, and it is positioned at 20*D* behind the propeller. The outer boundary is set at 4*D* from the propeller and symmetry boundary condition is used. The propeller surfaces are set as no-slip wall.

The computational domain is discretized using the hexahedral cells and the regions close to and behind the propeller are more refined. Prism layers are generated from the propeller surfaces to keep the non-dimensional wall distance y^+ below 1. This is because the boundary layer must be fully discretised for the transition model to activate. The computational domain and the generated mesh are shown in Figure 1.

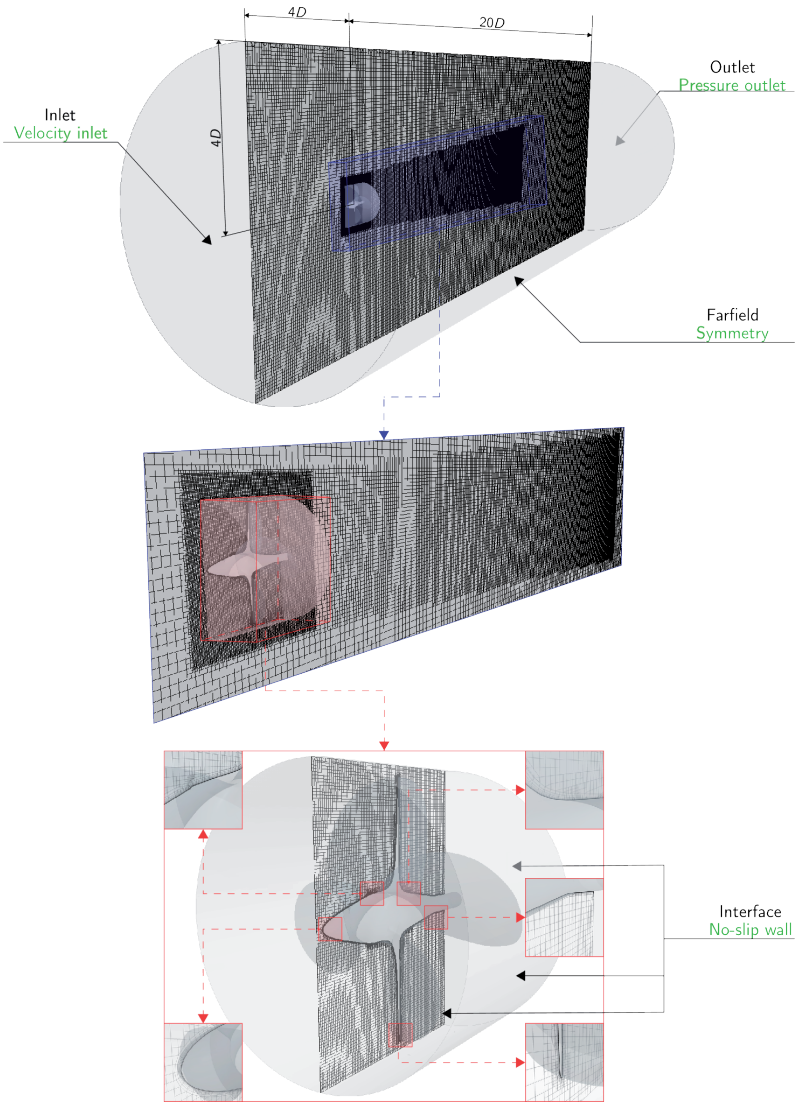

Fig. 1. The computational domain and the generated mesh.

The physical properties of water are set to freshwater conditions, consistent with the towing tank tests as: $\rho = 999.25\ \text{kg/m}^3$ and $\mu = 0.001191\ \text{Pa·s}$.

2.5 Geometry

The 3D model of the propeller was obtained using two methods: online generator and 3D scanning of the stock propeller. Since the analysed propeller is a Wageningen B-series propeller, the available online tool [13] was used for the generation of the 3D model of the propeller. To obtain the STL file of the 3D model, the only input required are the main parameters of the propeller. The graphical user interface is shown in Figure 2.

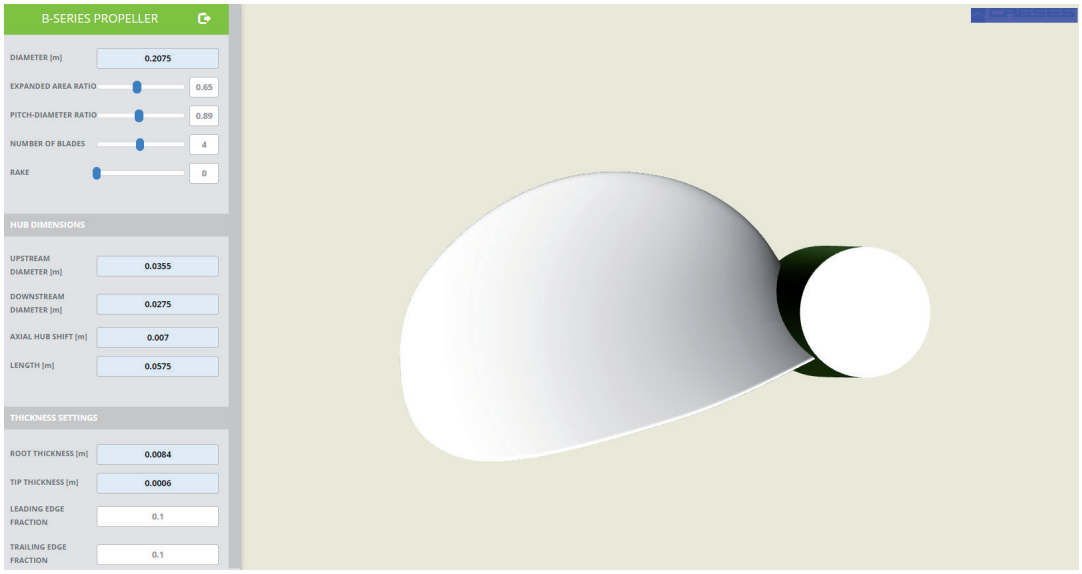

Fig. 2. Wageningen B-series online generator.

Since the stock propeller was available, the 3D scanning approach was employed using the ATOS 5x optical digitizer system [21]. The system comprises a scanning head equipped with a laser projector that generates a structured-light pattern. This pattern is projected onto the propeller surface and captured by high-resolution stereo cameras positioned at calibrated angles within the scanning head, as shown in Figure 3. To ensure measurement accuracy, the system incorporates real-time temperature compensation and adaptive exposure to account for environmental conditions and surface reflectivity variations. The resulting point cloud is generated through analysis and triangulation of the reflected light patterns using the Zeiss Inspect™ metrology software [22]. The propeller was coated with the surface treatment Reflecon Tarnish to obtain a uniform white surface, thereby improving the quality of the digitization process. The propeller was mounted on a rotating platform equipped with several uncoded circular markers with a diameter of 3 mm, as shown in Figure 4. Based on the acquired point cloud, a three-dimensional CAD model of the propeller was generated in STL format and subsequently smoothed for use in the numerical simulations.

Fig. 3. The 3D scanning process.

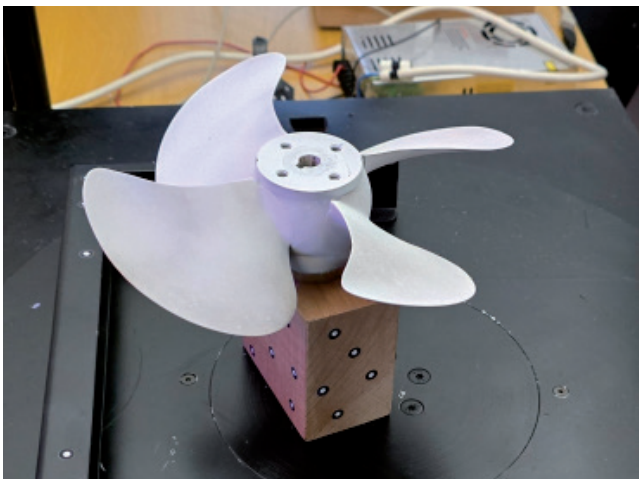

Fig. 4. The propeller situated on the rotating platform.

3. Results

3.1 Verification study

The verification study was performed to assess the numerical uncertainty due to mesh resolution using the Grid Convergence Index (GCI) method [23]. The calculation procedure for the *GCI* is provided by Grlj et al. [7]. It was necessary to calculate the grid spacing h to define the refinement ratio r between different mesh resolutions. Table 2 shows the obtained number of cells N and grid spacing h for each mesh size.

	Generated		Scanned	
	N	h, m	N	h, m
Coarse, 3	4.797M	9.00	1.734M	8.22
Medium, 2	6.088M	7.20	3.479M	5.81
Fine, 1	8.004M	5.83	8.001M	4.11

Table 2. Details of the meshes used in the verification study.

J	ε_{21}	ε_{32}	R	p	GCI_{fine}^{21}, %
0.08	0.0002	-0.0002	-1.36	0.877	0.83
0.16	0.0004	-0.0003	-1.17	0.448	1.52
0.24	0.0004	-0.0003	-1.39	0.956	0.43
0.32	0.0006	-0.0004	-1.45	1.062	0.46
0.40	0.0007	-0.0007	-1.04	0.125	4.40
0.48	0.0007	-0.0004	-1.85	1.775	0.18
0.56	-0.0004	-0.0005	0.70	1.038	0.18
0.64	-0.0004	-0.0005	0.73	0.908	0.19
0.72	-0.0006	-0.0009	0.71	0.997	0.27
0.80	-0.0019	-0.0026	0.73	0.908	0.89
0.88	-0.0053	-0.0056	0.95	0.145	23.89

Table 3. Results of the verification study for the generated propeller geometry.

The results of the verification study for the generated propeller geometry are shown in Table 3. The numerical uncertainty was calculated for the open water efficiency η_{O}. Monotonic convergence is achieved at $0.56 < J < 0.88$, while divergence is observed at lower J. The order of the method p is lower than 2, which suggests an overprediction of the *GCI*. Nevertheless, for most cases the calculated *GCI* is below 1 %, with only a few exceptions exhibiting higher values such as 1.51 % and 4.4 % at $J = 0.16$ and $J = 0.40$, respectively. The highest *GCI* is obtained at $J = 0.88$, however in this regime the η_{O} decreases rapidly. It should be noted that this operating region is not relevant to typical propeller performance, therefore, this point is considered an outlier and may be excluded from the verification study.

The results of the verification study for the scanned propeller geometry are shown in Table 4. Again, the numerical uncertainty was calculated for η_{O}. In this case, the obtained results are marginally better than those obtained for the generated propeller geometry. Monotonic convergence is obtained over almost the entire range of J. Slight oscillatory convergence is observed at $J = 0.08$, where p is well above 2, thus indicating an underprediction of the *GCI*. The obtained *GCI* is below 4 % for most cases, with the exception of the highest J, for which the *GCI* reaches 5.35 %. Excluding the lowest J, the minimum *GCI* value of 0.47 % is obtained at $J = 0.40$. Overall, both verification studies indicate that the fine mesh resolutions are adequate for the remaining numerical simulations.

J	ε_{21}	ε_{32}	R	p	GCI_{fine}^{21}, %
0.08	-0.00003	-0.0012	-0.03	10.569	0.001
0.16	-0.0010	-0.0018	0.55	1.711	0.82
0.24	-0.0018	-0.0023	0.79	0.696	2.96
0.32	-0.0018	-0.0031	0.57	1.603	0.79
0.40	-0.0018	-0.0038	0.49	2.090	0.47
0.48	-0.0027	-0.0043	0.63	1.324	1.07
0.56	-0.0036	-0.0050	0.73	0.927	1.94
0.64	-0.0042	-0.0059	0.72	0.944	2.04
0.72	-0.0048	-0.0067	0.71	0.982	2.07
0.80	-0.0070	-0.0097	0.72	0.942	3.10
0.88	-0.0098	-0.0132	0.74	0.864	5.35

Table 4. Results of the verification study for the scanned propeller geometry.

3.2 Validation study

In this subsection, the results of the validation study are presented. The relative deviations were calculated with the following equation:

$$RD = \frac{\phi_{\text{CFD}} - \phi_{\text{EFD}}}{\phi_{\text{EFD}}} \cdot 100\,\% \tag{7}$$

where ϕ is the considered physical quantity, and the subscripts CFD and EFD indicate that the results are obtained numerically and experimentally, respectively. First, the obtained results for both geometries and those obtained experimentally are compared in Figure 5. It is evident that the thrust coefficient K_T and torque coefficient K_Q obtained using the generated propeller geometry exhibit significant deviations from the experimental results. In contrast, numerical simulations performed with the scanned propeller geometry show improved agreement for both K_T and K_Q compared to those obtained with generated propeller geometry. However, the numerically predicted η_O differs significantly from the experimental values for both geometries, with the discrepancies increasing with J. The improved performance of the scanned geometry is attributed to the fact that, during the geometry generation process, certain input parameters had to be estimated due to the lack of precise measurements. Specifically, the authors did not have information on the rake angle, the leading and trailing edge fractions, or the size of the hub fillet. Moreover, the root and tip thicknesses were estimated based on the available drawings.

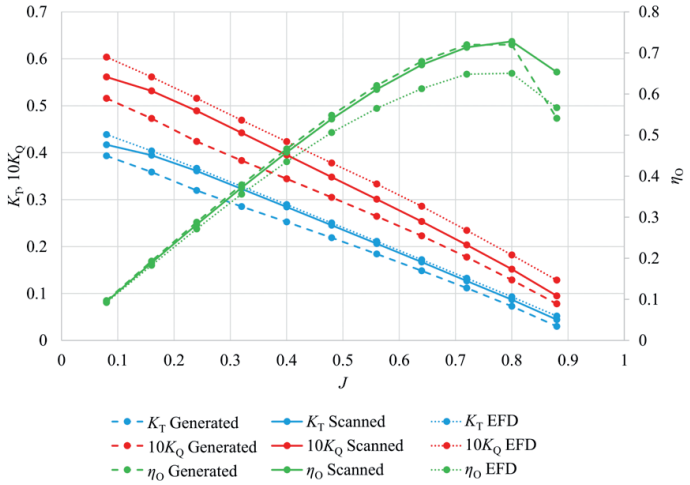

Fig. 5. Open water curves obtained numerically with generated and scanned propeller geometry, and experimentally.

The obtained relative deviations between the numerical and experimental results are given in Table 5. It can be seen that the relative deviations obtained between the numerical results with the generated propeller geometry and the experimental results are well above 10 % for both K_T and K_Q. The relative deviations for the scanned propeller are significantly lower than for the generated propeller. The relative deviations increase with J and the largest relative deviations are obtained for $J > 0.8$. However, this region is not relevant for typical propeller operating conditions.

	Generated			Scanned		
J	K_T, %	K_Q, %	η_O, %	K_T, %	K_Q, %	η_O, %
0.08	-10.38	-14.58	4.93	-4.99	-7.03	2.24
0.16	-11.13	-15.77	5.48	-2.24	-5.29	3.22
0.24	-12.83	-17.85	6.08	-1.49	-5.18	3.90
0.32	-13.07	-18.31	6.38	-1.64	-5.72	4.34
0.4	-12.84	-18.71	7.18	-1.82	-6.71	5.25
0.48	-12.67	-19.36	8.27	-2.00	-7.94	6.47
0.56	-12.8	-20.67	9.85	-2.29	-9.69	8.17
0.64	-13.62	-22.1	10.84	-2.89	-11.32	9.51
0.72	-15.85	-24.27	11.05	-4.39	-13.18	10.51
0.8	-21.56	-29.14	10.68	-6.65	-16.58	11.92
0.88	-42.03	-39.27	-4.61	-14.72	-26.03	15.27

Table 5. Relative deviations between the numerically and experimentally obtained results.

3.3 Flow visualization

In this subsection, more details of the obtained flow around the propeller at $J = 0.48$ are given. First, the obtained y^+ values on the propeller suction and pressure side are presented in Figure 6. For both geometries the y^+ values are below 1 across the entire propeller. In the case of the generated propeller geometry, y^+ values are marginally higher on the pressure side compared to those obtained for the scanned propeller geometry. This ensures that the boundary layer is fully resolved and that the transition model is active in the numerical simulations.

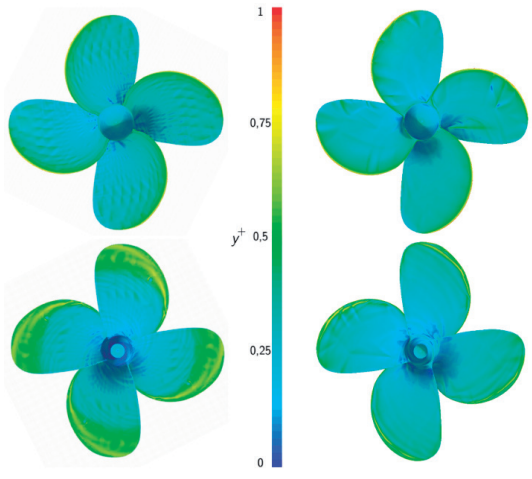

Fig. 6. The numerically obtained y^+ on the propeller suction (top) and pressure (bottom) side for generated (left) and scanned (right) propeller geometry.

Figure 7 presents the velocity magnitude distribution on the longitudinal cross section. It can be seen that the obtained velocity behind the propeller is higher in the case of the scanned propeller geometry compared to the generated propeller geometry. More details around the propeller are shown in Figure 8. The detailed view reveals that the transition between the blade and the hub is considerably smoother for the scanned propeller geometry than for the generated geometry. This is one of the factors contributing to the higher velocities observed downstream of the scanned propeller compared to those obtained with the generated propeller.

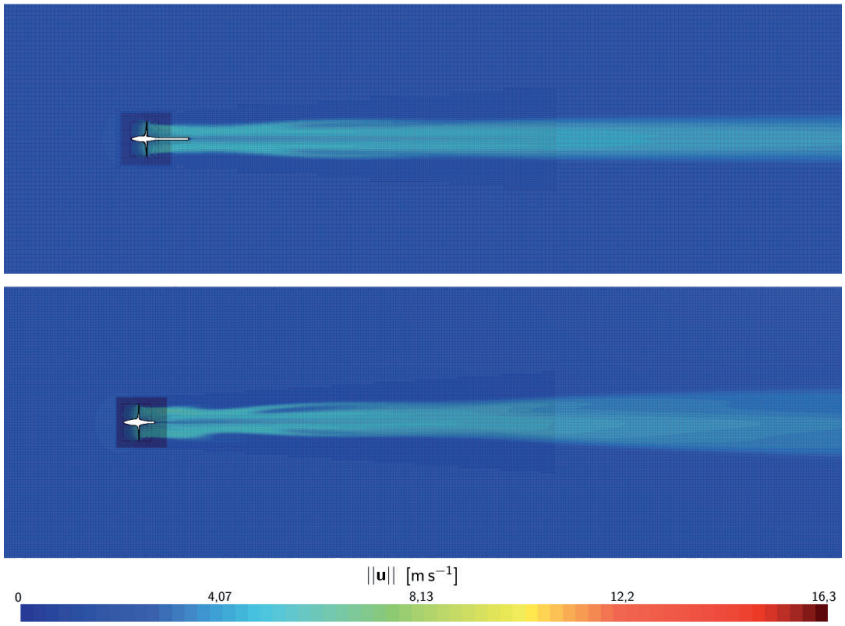

Fig. 7. The velocity magnitude on the longitudinal cross section obtained with the generated (top) and scanned (bottom) propeller geometry.

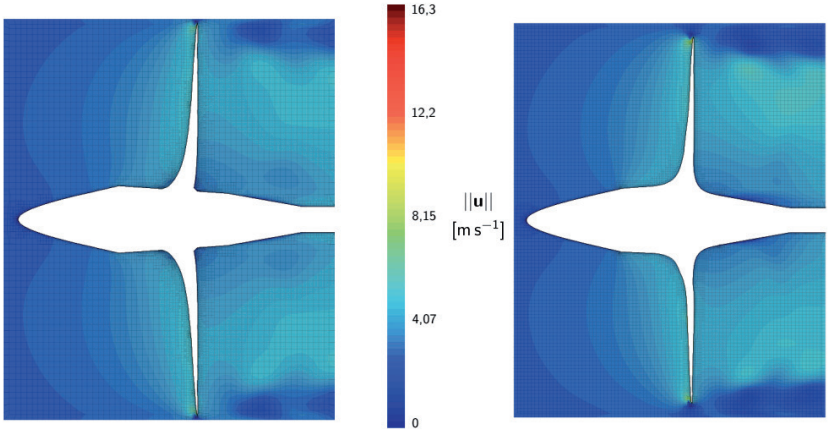

Fig. 8. Detailed view of the velocity magnitude around the generated (left) and scanned (right) propeller geometry.

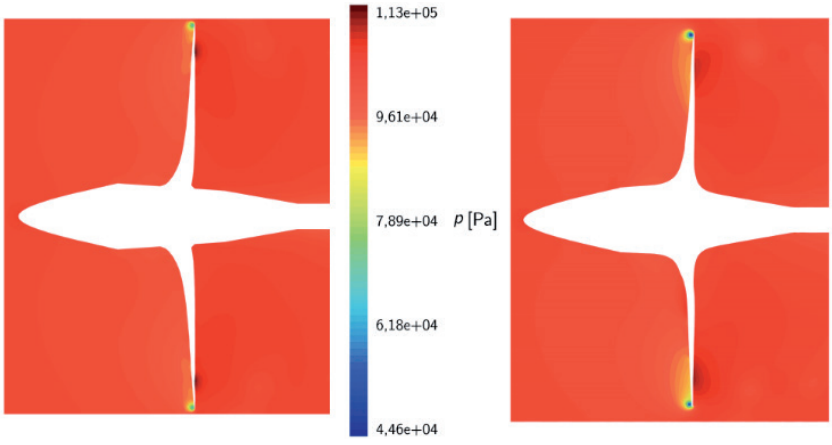

Fig. 9. Detailed view of the pressure around the generated (left) and scanned (right) propeller geometry.

Figure 9 shows the pressure fields around the propeller, with visible differences at the suction side on the propeller tips. Lower values are obtained for the scanned propeller compared to the generated propeller. Likewise, on the pressure side of the generated propeller the pressure is higher than for the case of the scanned propeller.

Lastly, the distribution of the skin friction coefficient C_f on the propeller surfaces are given in Figure 10. The differences between the results obtained with different propeller geometries are minimal. Slightly higher values of C_f are observed on the suction side of the scanned propeller compared to those of the generated propeller.

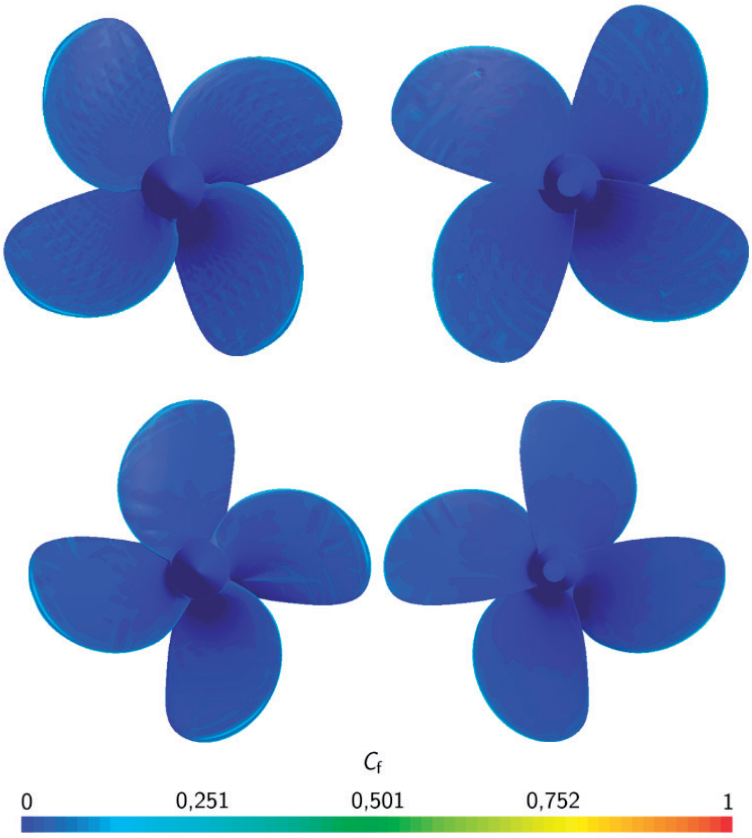

Fig. 10. Distributions of the skin friction coefficient on the suction (left) and pressure (right) side of the generated (top) and scanned (bottom) propeller geometry.

4. Conclusions

In this study, numerical simulations were performed to determine the open water characteristics for generated and scanned propeller. The mathematical model is based on the Reynolds Averaged Navier-Stokes equations and employs the Shear Stress Transport k-ω turbulence model in combination with the γ-$Re_{\theta t}$ transition model. The computational domain is discretized using the finite volume method within the commercial CFD software STAR-CCM+ 2310.

Two approaches to propeller geometry generation are considered: an automated approach with an online generator and 3D scanning of a stock propeller model. Verification of the numerical simulations is carried out using the Grid Convergence Index method. The verification procedure is applied for the open water efficiency of both propellers for the range of advance coefficient from 0.08 to 0.88. For the generated propeller, most *GCI* values are below 1 %, whereas slightly higher *GCI* values are observed for the scanned propeller. This confirms that the fine meshes are adequate for the rest of the numerical simulations.

Validation of the numerical results is performed through comparison with experimental data obtained at the Brodarski Institute in Zagreb. The results show that numerical simulations with the scanned propeller exhibit better agreement with the experimental data than those based on the generated propeller with respect to the thrust and torque coefficients. A direct comparison between the generated and scanned propeller reveals significant discrepancies in the thrust and torque coefficients, while the differences in open water efficiency are relatively small. These findings clearly indicate that the details of the actual propeller geometry have a substantial impact on the accuracy of numerical predictions.

Overall, this analysis confirms that computational fluid dynamics can be used to efficiently and reliably predict the propeller open water characteristics, provided that the propeller geometry is defined with sufficient accuracy.

5. Acknowledgement

This work was supported by the Croatian Science Foundation under the project number IP-2025-02-4779.

6. References

[1] Chen, X., Huang, Y., Wei, P., Zhang, Z., Jin, F. Numerical analysis of scale effect on propeller E1619. Proc. Int. Conf. Offshore Mech. Arct. Eng. - OMAE, 7B (2018)

[2] Shen, Z., Wan, D., Carrica, P. M. Dynamic overset grids in OpenFOAM with application to KCS self-propulsion and maneuvering. Ocean Eng. 108 (2015) 287-306

[3] Dogrul, A. Numerical prediction of scale effects on the propulsion performance of Joubert BB2 submarine. Brodogradnja 73(2) (2022) 17-42

[4] Dong, X. Q., Li, W., Yang C. J., Noblesse, F. RANSE-based simulation and analysis of scale effects on open-water performance of the PPTC-II benchmark propeller. J. Ocean Eng. Sci. 3(3) (2018) 186-204

[5] Farkas, A., Degiuli, N., Martić, I. The impact of biofouling on the propeller performance. Ocean Eng. 219 (2021) 108376

[6] Grlj, C. G., Degiuli, N., Farkas, A., Martić, I. Numerical Study of Scale Effects on Open Water Propeller Performance. J. Mar. Sci. Eng. 10(8) (2022) 1132

[7] Grlj, C. G., Degiuli, N., Martić, I. The Impact of Numerical Parameters on the Resistance Characteristics of a Container Ship at the Model and Full Scale. J. Mar. Sci. Eng. 11(9) (2023) 1672

[8] Grlj, C. G., Degiuli, N., Martić, I. Scale effects on the resistance and propulsion characteristics of the Japan Bulk Carrier. Ocean Eng. 339 (2025), 122059

[9] Liu, B., Vanierschot, M., Buysschaert, F. Comparison Study of the k − kL − ω and γ − Reθ Transition Model in the Open-Water Performance Prediction of a Rim-Driven Thruster. Int. J. Turbomach. Propuls. Power 9(1) (2024) 2

[10] Baltazar, J., Rijpkema, D., Falcão de Campos, J. On the use of the γ-Reθt transition model for the prediction of the propeller performance at model-scale. Ocean Eng. 170 (2018) 6-19

[11] Pawar, S., Brizzolara, S. Relevance of transition turbulent model for hydrodynamic characteristics of low Reynolds number propeller. Appl. Ocean Res. 87 (2019) 165-178

[12] Lopes, R., Eslamdoost, A., Johansson, R., RoyChoudhury, S., Bensow, R. E. A numerical study on the influence of crossflow transition on a marine propeller in open water. Ocean Eng. 310 (2024) 118573

[13] A. Friendship Systems. B-Series Propeller Generator.

URL:https://www.wageningen-b-series-propeller.com (23.1.2025.)

[14] Guan, G., Gu, W. Reconstruction of propeller and complex ship hull surface based on reverse engineering. J. Mar. Sci. Technol. 27(6) (2019) 0002

[15] Njaastad, E. B., Munthe-Kaas, N. H. Egeland, O. Robotic Autoscanning of Highly Skewed Ship Propeller Blades. IFAC-PapersOnLine 51(22) (2018) 435-440

[16] Njaastad, E. B., Steen, S., Egeland, O. Identification of the geometric design parameters of propeller blades from 3D scanning. J. Mar. Sci. Technol. 27(2) (2022) 887-906

[17] Zheng, L., Chen, S., Chen, X., Ji, S. Reverse Engineering-Inspired Parametric 3D Geometry Model of Marine Propeller. Pol. Marit. Res. 30(3) (2023) 35-47

[18] Brodarski Institute, "Report 6655-M. Resistance, self-propulsion and 3D wake measurement test results," Zagreb, 2022

[19] Degiuli, N., Martić, I., Pedišić-Buča, M., Grlj, C. G. Benchmark study on resistance and propulsion characteristics of a 6750-TEU container ship. Ocean Eng. 319 (2025) 120300

[20] ITTC, "Practical Guidelines for Ship Self-Propulsion CFD, ITTC 7.5-03-03-01.," ITTC-Recommended Procedures and Guidelines (2014)

[21] Zeiss. ATOS 5X.
URL: https://www.zeiss.com/metrology/en/systems/optical-3d/3d-scanning/atos/atos-5x.html (29.1.2025.)

[22] Zeiss. ZEISS Inspect.
URL: https://www.zeiss.com/metrology/en/software/zeiss-inspect.html (29.1.2025.)

[23] Eça, L., Hoekstra, M. A procedure for the estimation of the numerical uncertainty of CFD calculations based on grid refinement studies. Journal of Computational Physics. 262 (2014) 104-13

Ivan Sulovsky, Zoran Čarija, Anton Turk, Jasna Prpić-Oršić*

Insights into high-fidelity propulsion modelling in ship hydrodynamics

University of Rijeka, Faculty of Engineering, Vukovarska 58, Rijeka, 51000, Croatia
*Corresponding author: ivan.sulovsky@riteh.uniri.hr

Original scientific paper
Received: January 26, 2026
Accepted: April 27, 2026
https://doi.org/10.65776/ep.20.4.3

Abstract

This paper presents a Coupled Sliding Mesh (CSM) propulsion model for high-fidelity ship hydrodynamics simulations implemented within OpenFOAM. The model integrates rigid body motion with propeller rotation using Arbitrary Mesh Interface and morphing mesh approach. The model is validated against experimental data from self-propulsion tests on the Duisburg Test Case hull model at SINTEF, Norway, including calm water and three regular head wave cases. Grid comparative assessment demonstrated accurate capture of the self-propulsion point, with resistance deviating less than 1% from propeller thrust. Frequency domain analysis revealed successful capture of characteristic frequencies: wave encounter frequency, first shaft harmonic, and blade passing frequency. This study demonstrates that high-fidelity propulsion assessments can be achieved using open-source CFD tools for complex propeller-hull interaction problems.

***Keywords**: ship hydrodynamics, propeller modelling, OpenFOAM, CFD, self-propulsion*

1. Introduction

Computer power and numerical tools for ship hydrodynamics have developed rapidly in recent years. As a result, evaluating ship propulsion performance has shifted from traditional experimental testing toward computational approaches. Towing tanks, however, remain an indispensable asset that complements these computational tools. Among the available numerical methods, Computational Fluid Dynamics (CFD) based on Reynolds-averaging has become the dominant approach for solving a wide range of problems in ship hydrodynamics.

This paper addresses the modeling of propeller effects using a high-fidelity approach within the OpenFOAM toolbox [1]. OpenFOAM is an open-source CFD software based on a second-order collocated Finite Volume (FV) method. It has gained wide acceptance in research and academia due to its flexibility, allowing for extensive customization and user-developed improvements. Regarding the specific CFD modelling of the propeller effects, it is necessary to outline the most common methods used. The most straightforward approach represents propeller thrust and torque through virtual forces, eliminating the need to explicitly model the propeller geometry. These techniques fall under *body force* methods, alternatively referred to as actuator disk or virtual disk approaches. The core principle involves distributing forces within the propeller zone in a manner that remains consistent across different propeller designs. This consistency in force distribution was first examined nearly a century ago and given in [2], where findings continue to serve to this day for the body force group of methods.

The application of such propeller model has been successfully validated across many codes [3,4,5]. Since the main aim of this paper lies in a fully discretized propeller model in contrast to simplified body force method, an extensive review of the body force methods application is omitted. The most notable disadvantage of the body force methods is their inability to capture local flow features both upstream and downstream of the propeller plane. This is however compensated with high computational efficiency. A second group of methods for modelling propeller effects is based on a complete representation of propeller geometry with direct modelling of the rotation. Within the FV framework, propeller rotation can be modelled using overset technology [6,7] or via Arbitrary Mesh Interface (AMI) [8]. Also, a Moving Reference Frame (MRF) method is often applied in order to initialize the solution of the flow around the propeller [9,10].

In this paper, a novel numerical propulsion model is outlined that has been implemented in OpenFOAM code. The model is based on coupling motions between rigid body motion of the hull and a priori known rotating motion of the propeller, while using the advantages of both AMI interface and morphing mesh approach. The model is tagged with an acronym Coupled Sliding Mesh (CSM). Brief outline of the mathematical model of fluid flow is given in Section 2. In Section 3, experimental data with corresponding setup on the DTC hull model, originating from SINTEF, Norway is given. This is followed with a more detailed description of the CSM numerical propulsion model in Section 4. In Section 5, results of the self-propulsion tests in calm water and waves with propeller being modelled using CSM approach is given with a focus on the torque frequency content. While the CSM model and time-averaged self-propulsion results for the DTC hull have been previously reported by the authors [14], the present work extends that study through a systematic frequency-domain analysis of the propeller torque signal, identifying shaft harmonics and blade passing frequency components under calm water and regular head wave conditions. Lastly, conclusions and future work are outlined.

2. Mathematical model of fluid flow

In this Section, a mathematical model of fluid flow is given. Fluid flow is governed by Navier-Stokes (NS) equations for incompressible flows, the continuity equation (1) and momentum equation (2):

$$\nabla \cdot \mathbf{u} = 0 \tag{1}$$

$$\frac{\partial \mathbf{u}}{\partial t} + (\mathbf{u} \cdot \nabla)\mathbf{u} - \nu \nabla^2 \mathbf{u} = -\frac{1}{\rho}\nabla p + \mathbf{g} \tag{2}$$

where **u** represents the local fluid velocity. The left-hand side of the Navier-Stokes equation comprises three components: The total derivative representing temporal velocity changes, the convective transport term, and the viscous diffusion term. The term denotes the pressure gradient, g represents gravitational acceleration, and indicates the effective kinematic viscosity. To solve these governing equations, a multi-phase solver is employed, designed for two incompressible, isothermal, immiscible fluid phases (water and air). The air-water interface is captured using the Volume of Fluid (VOF) methodology, which introduces an indicator function α into the governing equations. This scalar field α modifies the Navier-Stokes equations by affecting the density ρ and effective kinematic viscosity, as shown in equations (3) and (4), respectively.

$$\rho = (1-\alpha)\rho_{air} + \alpha\rho_{water} \tag{3}$$

$$\nu = (1-\alpha)\nu_{air} + \alpha\nu_{water} \tag{4}$$

For accurate interface capturing, *isoAdvector* scheme is used [11]. The temporal discretization employs a first-order temporal scheme for calm water simulations while a second-order accurate backward scheme is set for transient simulations in waves. Convective fluxes are discretized using a linear scheme that transitions to an upwind-biased approach in regions with strong gradients, following the local flow direction. Diffusive gradient terms utilize Gaussian linear interpolation for their discretization. The pressure-velocity coupling is handled through the PIMPLE algorithm, configured with four iterations per time step: two dedicated to pressure residual reduction and two for the momentum equation solution.

Hydrodynamic coupling between the rigid body motion of the ship and the surrounding fluid is achieved using a six-degree-of-freedom solver, with constraints applied to the surge, sway, yaw, and roll motions. Mathematical closure of the Navier-Stokes equations, i.e., resolving turbulent fluxes, within the Reynolds-averaging concept is achieved using k-ω SST model. Regarding linear solvers, for solving large sparse matrices that are yielded from a FV mesh, a conjugate gradient (CG) method is chosen with a Cholesky preconditioner. Residual tolerance is set to 1^{-6}. Velocity components and turbulence terms are solved using a smooth solver, i.e., Gauss–Seidel smoother with a residual tolerance of 1^{-8}. With depiction of linear solvers this Section is concluded. Next Section outlines experimental data on the Duisburg Test Case (DTC) hull model in both calm water and regular head waves.

3. Experimental data

In this Section, experimental data using the DTC hull model, originally developed in [12] is presented. A comprehensive series of model tests was conducted at SINTEF in Trondheim, Norway, one of Europe's largest independent research institutions. Complete experimental procedures are documented in [13,14]. Rigid body motion tracking is performed using an Oqus optical positioning system, while propeller thrust and torque are recorded via a dynamometer. The reflective markers required for optical tracking, along with the umbilical cable supplying power and enabling data transmission, are visible in Figure 1.

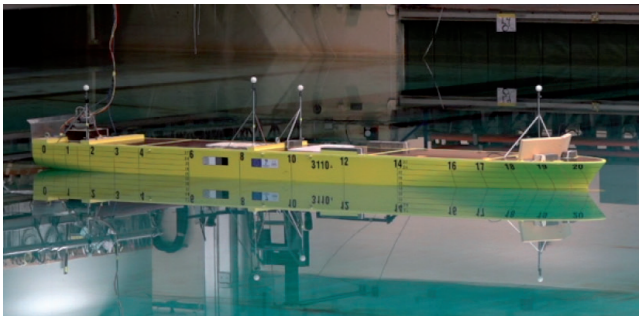

Fig. 1. DTC model. Reprinted with permission of the author [13,14]

Constructed at 1:63.65 scale, the model features a five-bladed fixed-pitch propeller and a twisted rudder equipped with a costa bulb. Rather than being towed, the ship operates in free-running mode, employing an autopilot system. Main particulars along with inertial characteristics of the model are shown in Table 1.

Main Parameter	Value
Scale, λ	63.65
Length between perpendiculars L_{PP} , m	5.577
Breadth B, m	0.801
Draught T, m	0.228
Displacement, Δ, kg	672.6
Pitch moment of inertia, I_{55} kgm^2	1266.3
Long. center of gravity, *LCG, m*	2.721

Table 1. DTC main parameters.

Self-propulsion test in calm water is performed at a propeller revolution rate of 11.5 rps with achieved speed of 1.03 m/s. Experiments in waves are performed at the same propeller revolution rate, under wave conditions listed in Table 2.

Wave case	1st	2nd	3rd
Wave height, H, m	0.06	0.087	0.119
Wave period, T, s	0.82	1.24	1.49
H/L_{PP}, -	0.011	0.0157	0.02
λ_e/L_{PP}, -	0.187	0.303	0.46

Table 2. Experimental conditions of self-propulsion tests in waves

Next Section deals with a numerical model developed within OpenFOAM framework with its main intention of enabling high-fidelity propulsion assessments.

4. Coupled Sliding Mesh (CSM) model

This Section describes the coupled sliding mesh model for hydrodynamic simulations utilizing both rigid body motions with propeller rotation. The new functionality is implemented in the existing OpenFOAM class that computes fluid-induced rigid body responses in CFD simulations. The main novelty in the CSM model is the coupled propeller rotation with rigid body motion, utilizing the usage of both AMI and morphing mesh. The main motivation for this numerical model is to avoid using overset mesh methodology which is based on volumetric interpolations of fields, opposing to the face-based interpolations that sliding mesh offers. A discretized propeller in the stern of the DTC model is shown in Figure 2.

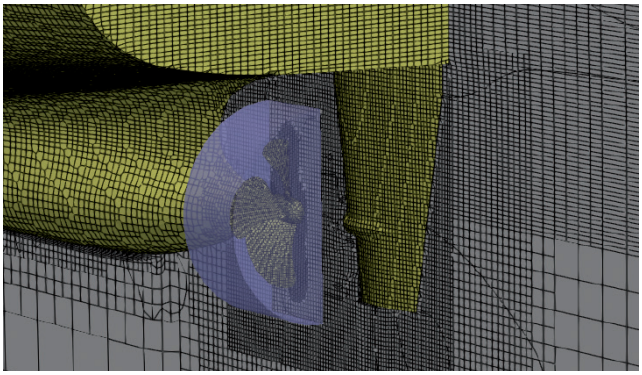

Fig. 2. Typical mesh topology for CSM model

Volumetric interpolations, as indicated in [15], are highly sensitive to the chosen interpolation procedure. Low-order interpolation scheme seem to cause mass imbalances within the domain which can have profound effects on the accuracy and validity of the simulations. High-order schemes perform slightly better, producing smoother fields, but are still prone to errors. Also, using overset mesh will inherently require significantly higher cell count. The usage of overset methodology is in some sense required when the geometries are complex and AMI interfaces are difficult to obtain. The main limitation of the model is that it does not overcome the well-known computational requirements necessary for any fully-resolving rotating geometries in CFD where the time step is dictated by the angle increment of the propeller within one iteration. This increment is usually of the order of 1°-5°, depending on the propeller rate of revolution. The computational workflow of the algorithm is given in Figure 3.

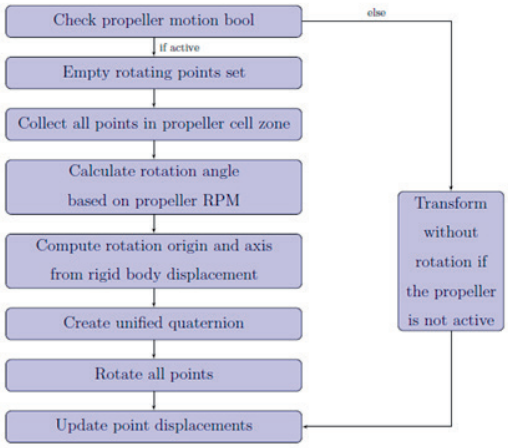

Fig. 3. Computational workflow of the CSM class

For the detailed description of the computational workflow and modifications to the existing OpenFOAM classes the interested reader is referred to [16].

5. Results and discussion

The results presented in this Section are partly given in author's previous work, presented in [17]. However, in this study, frequency content of the torque signal exhibited from the CSM model are explored further. In order to quantify the discretization errors, self-propulsion test in calm water is conducted on two grid sizes. The traditional grid sensitivity study is omitted due to high computational load of the simulations. In Figure 4, discretized stern region of the DTC hull along with the entire computational domain shown in Figure 5. The computational domain extends 1 ship lengths upstream, 3 lengths downstream, and 1 lengths in the transverse and vertical directions. The time-step size is set to 1 ms, corresponding to a propeller rotation increment of approximately 4° per time step. The inlet and oultet boundary conditions account for active wave generation [18]. For the frequency domain analysis, a DFT is applied over a window that corresponds to the wave encounter period using Hann window function.

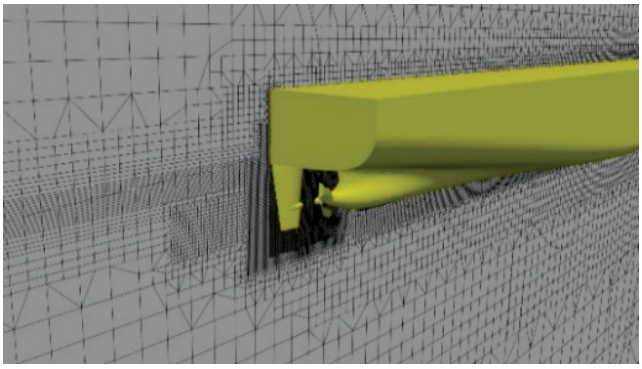

Fig. 4. Stern region of the DTC hull

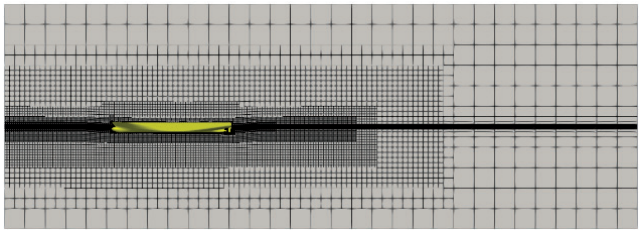

Fig. 5. Computational domain in transverse view

The results of the self-propulsion test in calm water, conducted on two grid sizes is given in Table 3. The coarse grid contains approximately 5.6 million cells and the fine grid 9.8 million cells. The refinement is applied uniformly with an approximate ratio of . The boundary layer is discretized in order to yield a non-dimensional distance commonly known as y+ around 30 for the flow around the hull while more stringent discretization is placed upon the propeller blades in order to achieve a value of 5.

	Experiment	Coarse grid	Fine grid
Thrust, *T,* N	14.126	14.965	14.321
Torque, *Q,* Nm	0.323	0.327	0.311

Table 3. Results of the self-propulsion test

It is important to emphasize that the self-propulsion point is correctly captured. The total resistance in both coarse and fine grid deviated no more than 1% compared to the propeller thrust. The swirling flow exhibited from the propeller motion, with colour scale showing the dimensionless flow speed is given in Figure 6

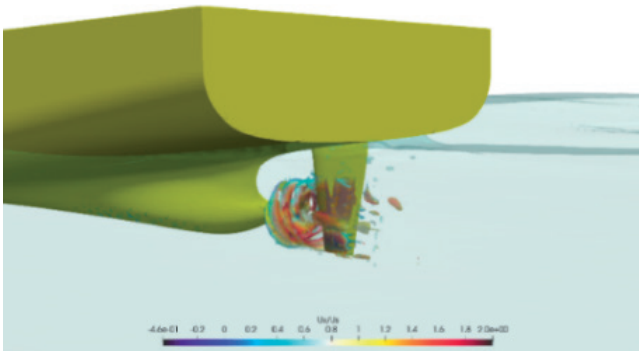

Fig. 6. Flow structures behind propeller

The comprehensive results of the self-propulsion in waves along with propeller-hull interactions are given in [19]. Instead, the focus of showcasing the results of self-propulsion tests is the frequency content that is embedded in torque signals of the propeller. The frequency content observed in the time domain signal of the propeller torque can be directly related to the propeller rotational characteristics [19,20]. For a propeller with N blades rotating at f_{rot}, the Blade Passing Frequency can be formulated as:

In the present case of the DTC hull operating with a five-bladed propeller at a frequency of 11.5 rps (Hz), the resulting BPF occurs at 57.5 Hz. In addition, shaft harmonics occur at integer multiples of the rotation frequency f_{rot}, formulated simply as:

Shaft harmonics are associated with non-uniform inflow and unsteady loading of the propeller in behind-hull conditions. The frequency content of the torque signal computed by CFD and experiment, across all three wave cases are given in Figures. 7., 8., and 9. respectively. The conversion from time to frequency domain has been done using Discrete Fourier Transform (DFT) method.

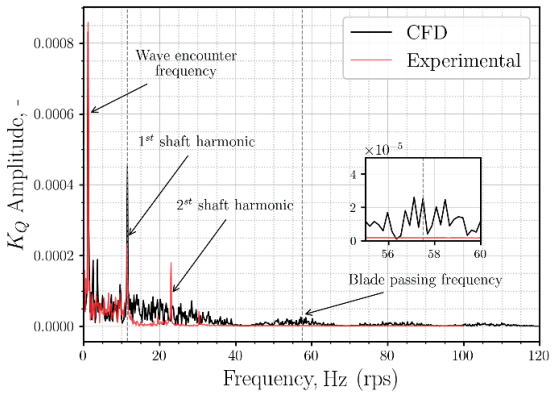

Fig. 7. Frequency content of the torque signal for the 1st wave case

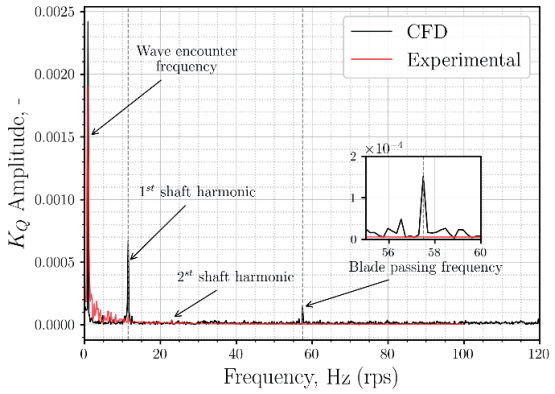

Fig. 8. Frequency content of the torque signal for the 2nd wave case

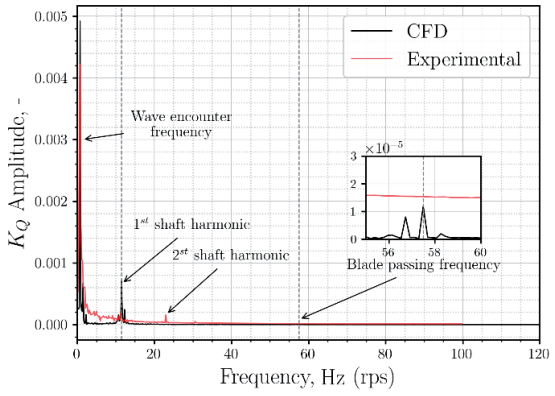

Fig. 9. Frequency content of the torque signal for the 3rd wave case

The frequency domain analysis of the propeller torque provides additional insight into the unsteady loading mechanisms acting on the propeller in waves, which cannot be fully assessed from time-averaged quantities alone. For all three wave cases, the dominant low-frequency peak corresponds to the wave encounter frequency, indicating that the propeller loading is strongly modulated by the incoming wave system. Across all cases, distinct peaks are observed at the first and second shaft harmonics, as well as at the blade-passing frequency. However, 2nd shaft harmonic is consistently captured in the experiment while only a slight peak from the CFD results is observed for case 2, Figure 7. This might be attributed to numerical noise or general polyhedral mesh discretization. The Blade Passing Frequency at 57.5 Hz occurs consistently in CFD computations for every case while it is not captured by the dynamometer in the experiments. Higher harmonics of the blade passing frequency were not captured both in CFD and experiments. While the dominant frequency peaks are correctly identified by the CFD model, amplitude discrepancies at higher frequencies, particularly beyond the first shaft harmonic are attributed to the current grid resolution and are considered acceptable given the simplified grid sensitivity that is performed.

These frequency components show that the CFD model captures both the large-scale unsteadiness from ship motion and wake non-uniformity, along with the high-frequency local blade loading effects. The CFD and experimental results agree well in identifying these characteristic frequencies, indicating that the main physical mechanisms are correctly represented. However, amplitude differences appear, particularly at higher frequencies. It is important to emphasize that the spatial discretization of the propeller blades has a significant impact on the exerted forces. In this study, an open-source tool *snappyHexMesh* is used, that is based on designing robust body-fitted polyhedral mesh around arbitrary geometries. For discretizing the propeller, strictly polyhedral cell type is not an ideal discretization approach, since it can produce artificially rough surface due to its polyhedral algorithm. The consequence of having polyhedral cells around the propeller blade can result in additional numerical noise due to summation of forces on cells that can exhibit significantly different face normals [21]. The advantages of block-structured mesh in reducing such numerical artifacts have been well documented [22], though their generation for complex propeller geometries remains a challenge. Nevertheless, in this work it is shown that even with open-source tools, a high-fidelity result can be yielded in complex propulsion assessment in ship hydrodynamics.

6. Conclusions

This paper presented a novel Coupled Sliding Mesh (CSM) propulsion model implemented within the OpenFOAM framework for high-fidelity ship hydrodynamics simulations. The model couples rigid body motion of the hull with propeller rotation using Arbitrary Mesh Interface (AMI) technology and morphing mesh approach, avoiding the volumetric interpolations inherent to overset methodologies that can introduce mass imbalances and require higher cell counts. The CSM model was validated against experimental data from self-propulsion tests on the DTC hull model conducted at SINTEF, Norway, covering both calm water and three regular wave cases. Grid comparative analysis on two mesh resolutions demonstrated that the self-propulsion point was correctly captured, with total resistance deviating no more than 1% from propeller thrust in both coarse and fine grids.

Frequency domain analysis of propeller torque signals revealed that the CSM model successfully captures the characteristic frequencies associated with propeller-hull interactions. For all wave cases, the dominant low-frequency peak corresponding to the wave encounter frequency was observed, indicating strong modulation of propeller loading by the wave system. The first shaft harmonic and blade passing frequency at 57.5 Hz were consistently captured in CFD results, demonstrating that the model correctly represents both large-scale unsteadiness from ship motion and high-frequency local blade loading effects. However, the second shaft harmonic and higher harmonics of the blade passing frequency showed weaker agreement with experiments, likely attributed to numerical noise, DFT parameters, and limitations of the polyhedral mesh discretization around propeller blades using *snappyHexMesh.* Despite these limitations, the study demonstrates that high-fidelity propulsion assessments in ship hydrodynamics can be achieved using open-source tools and the CSM approach, providing a viable alternative to overset methodologies for complex propeller-hull interaction problems.

Acknowledgments

This work was supported by the Croatian Science Foundation under the project HRZZ-IP-2022-10-2821.

This work was also supported by the University of Rijeka (PROJECTS no. PU-17 uniri-iz-25-10 - Funded by the European Union – NextGenerationEU).

References

[1] Weller, H.G., Tabor, G., Jasak, H., and Fureby, C. A tensorial approach to computational continuum mechanics using object-oriented techniques. Computer in Physics, 12(6):620–631,11 1998. ISSN 0894-1866. doi:10.1063/1.168744

[2] M. E. Goldstein. On the optimum velocity distribution for a propeller in axial flow. Journal of the Aeronautical Sciences, 2:1–12, 1929.

[3] Wang, H., Xiang, X., Xiang, G., Liu, C., Lichun and Yang, L. An improved body force method for simulation of self-propulsion auv with ducted propeller. *Ocean Engineering*, 281:114731, 2023. ISSN 0029-8018. doi: 10.1016/j.oceaneng.2023.114731

[4] Sulovsky, I., Mewes, S., El Moctar, O., and Prpić-Oršić, J. CFD study on a full-scale ship performance in a representative sea state. *Ocean Engineering*, 333:121519, 2025. ISSN 0029-8018, doi: 10./1016/j.oceaneng.2025.121519

[5] Yu, J., Yao, C., Liu, L. Application of virtual disk propulsion model for self-propelled surface ship in regular head wave. *Journal of Marine Science and Technology*, 28:471–495, 2023. doi: 10.1007/s00773-023-00935-8.

[6] Đurasević, S., Gatin, I., Uroić, T., and Jasak, H. Hydrodynamic performance of a full-scale ship with a pre-swirl duct: A numerical study with partially rotating grid method. *Ocean Engineering*, 283:115049, doi:10.1016/j.oceaneng.2023.115049

[7] Omar, N., Yoshiki, M., Yusuke, A., Sano, M., Hosogaya, K., and Maki, A. CFD based study on interaction between VecTwin rudders, propeller and hull during stopping maneuver and around hover region, Ocean Engineering, Volume 342, Part 1, 2025,ISSN 0029-8018, doi:10/1016/j.oceaneng.2025.122828

[8] P.E. Farrell, P.E. and Maddison, J.R. Conservative interpolation between volume meshes by local galerkin projection. *Computer Methods in Applied Mechanics and Engineering*, 200(1):89–100, 2011. ISSN 0045- 7825. doi: 10.1016/j.cma.2010.07.015.

[9] Ye, Z., Su, S., Zhou, L., Liu, Z. and Luo, X: Numerical study of water depth effects on the hydrodynamic performance of a shallow-water seismic survey ship's Z-drive ducted propeller. Brodogradnja 76 (4) (2025) 76401

[10] Kiss-Nagy, K. and Simongati, G. Digital twin of USV thruster based on CFD simulations and towing tank experiments. Brodogradnja 76 (4) (2025) 76403

[11] Roenby, J., Bredmose, H., and Jasak, H. A computational method for sharp interface advection. Royal Society Open Science, 3:160405, 2016.

[12] Shigunov, V., el Moctar, O. and Zorn, T. Duisburg test case: Post-panamax container ship for benchmarking. *Ship Technology Research*, 59(3):50–64, 2012. doi: 10.1179/str.2012.59.3.004.

[13] Øyvind Rabliås. *Numerical and Experimental Studies of Maneuvering in Regular and Irregular Waves*. PhD thesis, NTNU, Trondheim, 2022.

[14] Øyvind Rabliås, Ø. and Trygve, K. A rational model for maneuvering in irregular waves with the effect of waves on the propeller and rudder inflow taken into account. *Ocean Engineering*, 243:110186, 2022. ISSN 0029-8018, doi: 10./1016/j.oceaneng.2021.110186

[15] Lemaire, S.,Vaz, G., van Rijswijk, and Turnock, S.R. Influence of Interpolation Scheme on the Accuracy of Overset Method for Computing Rudder-Propeller Interaction. Journal of Verification, Validation and Uncertainty Quantification, 8(1):011002, March 2023. doi: 10.1115/1.4056681.

[16] Sulovsky, Ivan. *Numerical modelling of ship propulsion characteristics in sea waves: doctoral thesis*. Diss. Sveučilište u Rijeci, Sveučilište u Rijeci-Tehnički fakultet, Zavod za brodogradnju i inženjerstvo morske tehnologije, 2026.

[17] Sulovsky, I., Bakica, A. and Prpić-Oršić, J: CFD assessment of ship propulsion and propeller-hull interactions in waves using low and high fidelity approach. *Ocean Engineering,* 346:123843, 2026. ISSN 0029-8018. doi: 10/1016/j.oceaneng.2025.123843

[18] Higuera, P., et al., 2013. Realistic wave generation and active wave absorption for navier-Stokes models: application to openFOAM®. Coastal Eng. 71, 102–118. https://doi.org/10.1016/j.coastaleng.2012.07.002

[19] Witte, M., Nolte, N., Hinnenhal J. and Wurm, F.H. Hydroacoustic investigations of a marine propeller based on holography. *Ocean Engineering,* 345:123231,2026, ISSN:0029-8018. doi:10.1016/j.oceaneng.2025.123231

[20] Ebrahimi, A., Seif, M.S., Nouri-Borujerdi, A. Hydrodynamic and Acoustic Performance Analysis of Marine Propellers by Combination of Panel Method and FW-H Equations. *Math. Comput. Appl.* 2019, *24*, 81. https://doi.org/10.3390/mca24030081

[21] Bakica, A., Vladimir, N. and Koričan, M. Propeller retrofit on a fishing vessel: Self-propulsion CFD simulations with exisiting and new propeller. Sustainable Development and Innovations in Marine Technologies. 2025

[22] Sikirica, A. Čarija, Z. Kranjčević, L. and Lučin, I. Grid Type and Turbulence Model influence on Propeller Characteristics Prediction. *J. Mar. Sci. Eng.* 2019, *7*, 374.

Marijana Marjanović[1,], Jasna Prpić-Oršić[1], Marko Valčić[1,2]*

Propagation of weather forecast uncertainties through attainable ship speed prediction models

[1] University of Rijeka, Faculty of engineering, Vukovarska 58, Rijeka, 51000, Croatia
[2] University of Zadar, Maritime Department, Ruđera Boškovića 5, Zadar, 23000, Croatia
[*] Corresponding author: marijana.marjanovic@riteh.uniri.hr

Original scientific paper
Received: January 25, 2026
Accepted: April 16, 2026
https://doi.org/10.65776/ep.20.4.4

Abstract

Accurate prediction of weather-induced ship speed loss requires understanding how meteorological forecast uncertainties propagate through vessel performance models. This study presents a comparative assessment of three computational approaches for attainable speed estimation: the Wärtsilä NTPRO 5000 navigation simulator with JONSWAP and Pierson-Moskowitz spectral implementations, and HydroComp NavCad hydrodynamic software. Over 2,000 simulations were conducted for a 28,050 DWT bulk carrier across varying wave heights (0-12 m), encounter angles (0°-180°), and operational speeds (12.0-14.5 knots). Correlation analysis between meteorological predictor variables and ship speed response uncertainties revealed that significant wave height errors exhibit the strongest coupling with speed prediction errors (r = 0.65-0.97), while encounter angle geometry substantially modulates uncertainty propagation patterns. The Pierson-Moskowitz implementation demonstrated the most balanced error characteristics, whereas JONSWAP produced more polarised correlations at extended forecast horizons. Results indicate that uncertainty quantification approaches must account for both model-specific sensitivities and spatially varying forecast skill degradation.

***Keywords**: Weather forecast degradation; Attainable speed modelling; Uncertainty quantification; Correlation analysis.*

1. Introduction

The attainable ship speed under varying weather conditions has been studied using empirical and semi-empirical methods [1,2], physics-based approaches [3,4], and, more recently, data-driven and intelligent models [7,8]. These methods have enabled increasingly accurate speed prediction and demonstrated the potential for substantial fuel savings and emission reductions through weather-aware optimisation [5,6]. Multi-objective frameworks [9], deep reinforcement learning for routing [10], and adaptive control strategies [11] further extend these capabilities. However, most of these approaches remain deterministic and do not account for the propagation of forecast errors through vessel response models.Although uncertainty sources in ship routing have been extensively reviewed [12], existing probabilistic frameworks are typically first-order and rely on linearization [13], which is inadequate for highly nonlinear ship responses. Links between ensemble forecast uncertainty and fuel consumption have been explored [14], yet often with simplified resistance models. Uncertainty has also been recognised in collision avoidance and trajectory prediction [15], underscoring its relevance across maritime operations. While forecast errors are known to grow non-linearly with lead time [5], their transformation through ship performance models remains insufficiently characterised. Most existing frameworks still treat weather forecasting and ship performance as independent components, neglecting the coupled interactions that govern voyage-level uncertainty. This study addresses these limitations by systematically quantifying how meteorological forecast uncertainties propagate through three distinct ship performance modelling approaches. The primary contributions include: (i) comparative uncertainty analysis across Wärtsilä NTPRO 5000 navigation simulator implementations utilizing both JONSWAP and Pierson-Moskowitz spectral formulations, alongside HydroComp NavCad hydrodynamic software; (ii) correlation analysis establishing quantitative relationships between predictor variable (meteorological) and response variable (ship speed) uncertainties across varying sea states and encounter geometries; and (iii) practical demonstration of the framework through a transatlantic case study incorporating estimated time of arrival uncertainty quantification under realistic winter North Atlantic conditions.

2. Ship Performance Simulation Framework

Quantifying attainable ship speed under stochastic weather conditions requires reliable computational tools that capture the interactions between ship hydrodynamics and environmental forces. This study employs three distinct modelling approaches to generate comprehensive speed-loss predictions, enabling a comparative assessment of uncertainty-propagation characteristics.

2.1. Data collection using simulations

Two complementary computational environments were employed for attainable ship speed prediction, representing fundamentally different modelling paradigms.

The Wärtsilä NaviTrainer NTPRO 5000 full-mission bridge simulator served as the primary experimental platform. This DNV Class A-certified system solves vessel motion equations in real time across six degrees of freedom, capturing complex interactions among hull hydrodynamics,

propulsion forces, and environmental disturbances [16,17]. Hydrodynamic forces are decomposed into positional and damping components, determined from experimentally derived coefficients obtained from tank tests. Environmental loading is computed using distinct models for wind and wave effects, with wave-induced forces comprising first-order oscillatory components and second-order mean drift forces that contribute to steady speed loss. Two spectral formulations were implemented: the Pierson-Moskowitz spectrum for fully developed seas and the JONSWAP spectrum for fetch-limited conditions [18].

Throughout simulations, an autopilot system maintained commanded heading rather than track-keeping mode, while speed loss emerged naturally from the force balance between thrust and environmental loading. This configuration was chosen deliberately: the lookup tables are intended to characterise the intrinsic wind–wave-induced speed loss for each encounter geometry, isolated from the additional rudder-activity losses that occur when a vessel compensates for drift along a predefined track. In operational routing, such track-keeping losses and drift-induced heading corrections can be superimposed on the lookup-table values as separate corrections at the routing stage.

Parallel simulations utilised HydroComp NavCad, employing quasi-static resistance decomposition methods based on ITTC-1978 correlation procedures [19, 20]. Unlike the time-domain NTPRO approach, NavCad separates total resistance into distinct physical components such as bare-hull viscous resistance, wave-making resistance, appendage drag, and environmental added resistance, which are individually computed and summed. Wave-added resistance predictions employ regression-based methods derived from systematic model test series, with the Aertssen approach [21] enabling direct speed-loss estimation for weather-routing applications.

2.2. Reference vessel and simulation matrix

A 28,050 DWT bulk carrier served as the reference vessel for all simulations, selected for its representative characteristics among medium-sized commercial cargo ships operating transatlantic routes [22]. The principal particulars are summarised in Table 1.

Table 1. Principal particulars of the reference bulk carrier

Parameter	Value	Unit
Length between perpendiculars (LPP)	160.40	m
Beam (B)	27.20	m
Depth (D)	13.60	m
Design draft (T)	9.819	m
Deadweight (DWT)	28,050	tons
Gross tonnage (GT)	17,009	-
Main engine power (MCR)	6,150	kW
Propeller diameter	5.25	m
Service speed	~14.0	knots

The propulsion system consists of a two-stroke marine diesel engine rated at 6,150 kW at 136 rpm under nominal conditions, derated to 5,850 kW at 129 rpm for heavy fuel oil operation. Power transmission is achieved through a direct-drive shaft system connected to a four-bladed fixed-pitch propeller with a mean pitch of 3.686 m and a 35-degree skew angle optimised for bulk carrier operations. These specifications were integrated into both computational platforms to ensure consistent representation of vessel response characteristics.

The simulation matrix was designed to comprehensively cover operationally relevant conditions encountered on North Atlantic routes. Environmental parameters included:

(*i*) Significant wave heights: 13 wave heights spanning $H_S \in \{0, 1, 2, ..., 12\}$ metres, corresponding to WMO Sea State Codes 0-8

(*ii*) Wave encounter angles: 13 orientations $\alpha_{waves} \in \{0°, 15°, 30°, ..., 180°\}$ covering head seas (0°), bow-quartering (15°-75°), beam seas (90°), stern-quartering (105°-165°), and following seas (180°)

(*iii*) Intended reference ship speeds: $V_{ref.} \in \{12.0, 13.5, 14.5\}$ knots

(*iv*) Loading conditions: Full load and ballast configurations

(*v*) Wave spectra: Pierson-Moskowitz and JONSWAP.

Wind speed was not varied as an independent parameter but was coupled to significant wave height through the Beaufort–Douglas sea-state correspondence, consistent with the fully developed sea assumption of the Pierson–Moskowitz spectrum and the wind–wave coupling intrinsic to the JONSWAP formulation. Wind direction was kept aligned with the wave direction, reflecting typical North Atlantic conditions in which swell and wind sea co-propagate; this simplification is the same as that adopted in the underlying simulation framework [23]. This parameterisation yielded 2,028 unique simulation scenarios for NTPRO 5000 (accounting for both spectral formulations and loading conditions) and 1,014 scenarios for NavCad (single spectral treatment) [23]. While simulations were conducted for encounter angles 0°-180°, results were extended to the full 360° range by applying symmetry principles, as port and starboard wave encounters produce mirror-image responses.

2.3. Attainable Speed Formulation

Neglecting ocean current effects, the attainable ship speed $V_{att.}$ can be expressed as a function of intended reference speed and prevailing sea state conditions

$$V_{\text{att.}} = f\left(V_{\text{ref.}}, H_S, T_p, \alpha_{\text{waves}}\right) \quad (1)$$

where $V_{ref.}$ denotes the intended reference speed (knots), H_S represents significant wave height (m), T_p indicates peak wave period (s), and α_{waves} specifies the encounter

wave angle (degrees). The functional relationship is determined empirically, with results organised into lookup tables that enable rapid interpolation for arbitrary input combinations.

The sea conditions can be actual, for actual values of $H_S^{(act.)}$, $T_P^{(act.)}$ and $\alpha_{waves}^{(act.)}$, and forecasted, for forecast values of $H_S^{(for.)}$, $T_P^{(for.)}$ and $\alpha_{waves}^{(act.)}$. The attainable ship speed $V_{att.,actual}$ in actual conditions is

$$V_{att.,actual} = f\left(V_{ref.}, H_S^{(act.)}, T_P^{(act.)}, \alpha_{waves}^{(act.)}\right) \quad (2)$$

i.e. the predicted attainable ship speed $V_{att.,predicted}$ in forecasted conditions is

$$V_{att.,predicted} = f\left(V_{ref.}, H_S^{(for.)}, T_P^{(for.)}, \alpha_{waves}^{(for.)}\right) \quad (3)$$

For operational implementation, attainable speed values are obtained through bilinear interpolation between discrete simulation points, ensuring smooth transitions for intermediate wave heights and encounter angles. The encounter wave angle is computed from ship heading ψ and meteorological wave direction β_{waves} according to

$$\alpha_{waves} = \begin{cases} \beta_{waves} - \psi, & for\ \psi \le \beta_{waves} \\ 2\pi + \beta_{waves} - \psi, & for\ \psi > \beta_{waves} \end{cases}. \quad (4)$$

While the theoretical formulation for attainable ship speed includes peak wave period T_p as an independent variable, practical implementation couples period to significant wave height through the spectral relationships. In the Pierson-Moskowitz formulation, peak period is not independently controllable but rather a derived quantity determined by the spectrum parameterisation. Similarly, JONSWAP implementation maintains period-height coupling through wind-wave relationships. This simplification reflects the physical reality that wave height and period evolve together according to fetch, duration, and wind speed characteristics [18], and is justified for the North Atlantic routes studied (e.g., Rotterdam–New York), where swell and wind seas typically align.

Simulation outputs occasionally yielded undefined (NaN) values representing sea states where the autopilot system could no longer maintain the demanded course, i.e. conditions characterised by excessive yaw rates, severe roll and pitch amplitudes, or loss of directional stability. These values effectively define operational boundaries beyond which navigation becomes hazardous, serving as indicators for route optimisation algorithms to identify avoidance zones or mandate course and speed alterations.

3. Weather Forecast Uncertainty

The meteorological dataset was organised into four forecast lead-time classes, each aligned with a distinct level of operational decision-making. The short-range window (0–24 h) represents immediate onboard planning and was sampled at 0, 6, 12, 18, and 24 hours. Tactical voyage adjustments are supported by the medium-range window (24–72 h), comprising forecasts at 30, 36, 42, 48, 54, 60, 66, and 72 hours. The extended-range horizon (72–120 h) addresses strategic routing decisions and includes predictions at 78, 84, 90, 96, 102, 108, 114, and 120 hours. Finally, the long-range window (120–168 h) provides advance planning capability through outputs at 126, 132, 138, 144, 150, 156, 162, and 168 hours. This structured temporal partitioning enables a systematic evaluation of forecast skill decay with increasing lead time, which is essential for analysing how uncertainty propagates into attainable ship speed estimates.

For each lead-time class, both forecasted and observed values were collected for six meteorological variables directly influencing ship performance: significant wave height H_s (m), representing the mean height of the highest one-third of waves; peak wave period T_p (s), characterising the dominant spectral component; wind speed V_{wind} (m/s) at the 10 m reference level; wave direction β_{waves} (deg), defined as the direction from which waves propagate relative to geographic north; wind direction β_{wind} (deg), defined analogously for the atmospheric flow; and the encounter angle α_{waves} (deg), describing the relative orientation between vessel heading and incoming wave direction.

All data processing and uncertainty analysis were implemented within a Python-based workflow tailored for large-scale meteorological datasets, employing specialised libraries (cfgrib and eccodes for GRIB decoding, xarray and pandas for spatio-temporal alignment, and NumPy, SciPy and scikit-learn for statistical evaluation) within Python 3.13.

4. Uncertainty metrics

The Root Mean Square Error (RMSE) [24], can be defined as

$$RMSE = \sqrt{\frac{1}{n}\sum_{i=1}^{n}(F_i - O_i)^2}. \quad (5)$$

The quadratic form of the RMSE places a disproportionately high weight on large deviations, rendering the metric especially responsive to sporadic but severe errors. This property is advantageous for revealing extreme discrepancies in predicted ship speed that may have a decisive influence on routing outcomes and schedule reliability.

In contrast, the Mean Absolute Error (MAE) offers a linear measure of the average error magnitude [24] and is defined as

$$MAE = \frac{1}{n}\sum_{i=1}^{n}|F_i - O_i|. \quad (6)$$

Bias quantifies systematic forecast tendencies, which reveals if a model consistently over- or under-predicts, and is noted as [25]

$$\text{Bias} = \frac{1}{n}\sum_{i=1}^{n}(F_i - O_i)\,. \tag{7}$$

Unlike RMSE and MAE, the bias may approach zero even in the presence of substantial errors, provided that positive and negative deviations compensate each other. Consequently, bias must be evaluated in conjunction with magnitude-based metrics in order to discriminate between true predictive accuracy and mere cancellation of opposing errors [25].

The Index of Agreement (Willmott's Index) [26] is a normalised metric ranging from 0 to 1 that quantifies the degree of correspondence between model predictions and observations relative to their variability. It is defined as

$$\text{IoA} = 1 - \frac{\sum_{i=1}^{n}(F_i - O_i)^2}{\sum_{i=1}^{n}(|F_i - \bar{O}| + |O_i - \bar{O}|)^2}. \tag{8}$$

The Fractions Skill Score (FSS) is a spatial verification metric for high-resolution forecasts of threshold-based events [27]. Ranging from 0 (no skill) to 1 (perfect agreement), it evaluates forecast performance by comparing the fractional occurrence of an event within local neighbourhoods rather than at individual grid points. Forecast and observed fields are first binarised, after which a moving window computes the local event fractions in both fields. The FSS is then defined as [27]

$$\text{FSS} = 1 - \frac{\text{MSE}_f}{\text{MSE}_{f,ref}} = 1 - \frac{\sum_{n=1}^{N}[O(n)-F(n)]^2}{\sum_{n=1}^{N}[O^2(n)+F^2(n)]} \tag{9}$$

where MSE_f denotes the mean squared error between the forecast fractions $F(n)$ and the observed fractions $O(n)$ for neighbourhoods $n = 1,\ldots,N$, and $\text{MSE}_{f,ref}$ is the reference MSE corresponding to a no-skill forecast, i.e. the worst-case scenario. Here, N denotes the total number of neighbourhoods.

The Continuous Ranked Probability Score (CRPS) generalises forecast verification to probabilistic predictions by evaluating the agreement between a forecast distribution and the corresponding observed value [28]

$$\text{CRPS} = \sigma\left[z(2\Phi(z) - 1) + 2\phi(z) - \frac{1}{\sqrt{\pi}}\right] \tag{10}$$

where $\sigma=\alpha\,|\,f\,|$ is the assumed standard deviation, is the uncertainty factor (10 % by default), f is the forecast value, $z = \frac{O-\mu}{\sigma}$ is the standardised difference, O is the actual observed value, $\Phi(z)$ is the standard normal cumulative distribution function (CDF), and

$$\phi(z) = \frac{1}{\sqrt{2\pi}}e^{-\frac{z^2}{2}} \tag{11}$$

is the standard normal probability density function (PDF). CRPS generalises the Mean Squared Error to probabilistic forecasts by evaluating entire predictive distributions [28]. A value of zero is ideal and occurs when all probability is assigned to the observed outcome [28,29]. For deterministic forecasts, CRPS reduces exactly to MAE, making it a proper scoring rule that reflects both accuracy and uncertainty.

The Uncertainty Growth Rate (UGR) measures how forecast uncertainty increases with lead time, providing insight into the limits of predictability [30]. A linear form of UGR may be distinguished

$$\text{UGR}_{\text{lin.}}(h) = \frac{\text{d}\big(\text{RMSE}(h)\big)}{\text{d}h} \tag{12}$$

where RMSE(h) is theRMSE at lead time h, Nh, is the number of forecast observation pairs at lead time h, $F_i^{(h)}$ is the i-th forecast value at lead time h, is the i-th observed value.

For directional quantities such as meteorological wave direction and encounter wave angle, uncertainty was quantified using the Circular Mean Absolute Error, defined as

$$\text{CMAE} = \frac{180}{\pi}\cdot\frac{1}{n}\sum_{i=1}^{n}|\text{atan2}(\sin\Delta_i, \cos\Delta_i)| \tag{13}$$

It accounts for the circular nature of angles, ensuring that only the smallest directional difference is evaluated.

5. Uncertainty Analysis

For every location and time, a forecast–observation pair is formed by combining the forecasted value with the corresponding observed value of the same variable. These pairs are grouped in their respective sea-state bins.

Over the analysed four-month period (January–April 2025), each bin accumulates a large number of such pairs, from which uncertainty metrics are computed. This approach assumes that forecast errors within a given sea state are statistically stationary and independent of geographic location, temporal evolution, and synoptic regime. Although temporal correlations are not preserved when grid points transition between bins, this methodology is well aligned with ship routing practice. A vessel encounters sea states spatially along its route rather than at fixed locations, and routing decisions therefore require error statistics that are conditioned on sea state rather than on position. Spatial pooling provides robust statistics for each sea state while remaining computationally efficient.

The non-directional variables exhibit systematic forecast degradation with lead time for significant wave height, wave period, and wind speed. For wave height, RMSE increases from approximately 0.05–0.12 m at 24 h to 0.64–1.04 m at 168 h in moderate seas, showing near-linear growth, while severe sea states display accelerated

error growth beyond 72 h. MAE remains about 15–20 % lower than RMSE across all conditions, indicating the persistent presence of operationally relevant outliers. In calmer seas, relative uncertainty becomes pronounced despite small absolute errors, whereas in higher sea states, predictability limits emerge at longer horizons.

Wave period forecasts are markedly more stable, with RMSE increasing from roughly 0.11–0.17 s at 24 h to 1.16–1.40 s at 168 h in moderate conditions, and exhibiting weaker dependence on sea state. Probabilistic verification confirms good calibration throughout. These patterns demonstrate that forecast uncertainty evolves in a variable- and sea-state-dependent manner, providing a necessary basis for analysing its propagation into attainable ship-speed predictions.

Wind speed exhibits the highest relative uncertainty among all analysed variables. In moderate seas, RMSE increases from approximately 0.45–0.85 m/s at 24 h to 3.04–4.37 m/s at 168 h, while in higher sea states it can exceed 8.0 m/s at maximum lead times. The associated exponential UGR of about 1.3–1.45 % per hour is comparable to the 1.5–1.8 % observed for wave height, indicating similar predictability limits. Across all variables, forecast uncertainty shows a non-linear dependence on sea state. Although absolute errors generally grow with severity, relative uncertainty follows a U-shaped pattern, with the largest values in very calm and extreme conditions. This demonstrates that forecast reliability depends not only on lead time but also on environmental intensity.

Directional variables require circular metrics, with CMAE accounting for angular discontinuity. An example of results is shown in Figure 1. Wind direction variability differs markedly across sea states: in moderate seas, CMAE increases from about 3.5–4.8° at 24 h to 38–46° at 168 h, while in calm conditions it can exceed 50° even at short lead times. In severe weather, stronger atmospheric forcing yields 20–30 % lower CMAE than in moderate seas. The steepest growth occurs in the 24–72 h window, where CMAE increases by 5–20°, coinciding with key tactical planning horizons. Wave direction forecasts are markedly more stable. In moderate seas, CMAE grows from roughly 1.3–3.4° at 24 h to 16.6–31.4° at 168 h, with calm conditions reaching about 40° only at long lead times. In sea states 6–9, CMAE remains below 30° even at extended horizons. Encounter wave angle exhibits the most complex behaviour, with CMAE ranging from 1.3–3.4° at 24 h to 16.6–31.4° at 168 h in moderate seas. Uncertainty is up to 40 % higher in following seas than in head seas, as small directional errors can shift conditions from benign to hazardous. In sea states above 7, CMAE may increase by up to 25° within a single 24-hour update, indicating predictability barriers not captured by current ensemble systems and highlighting a critical asymmetry for route optimization.

Cross-correlation analysis shows that encounter-angle uncertainty cannot be approximated as a linear combination of wind and wave direction errors. Their coupling varies strongly with sea state, with correlation coefficients increasing from about 0.3 in calm conditions (sea states 0–2) to 0.85 in storms (sea states 7–9), reflecting the dominance of unified atmospheric systems in severe weather. When combined with the inherent 15° heading variability of autopilot control, this interaction produces compound uncertainties that exceed root-sum-square estimates by 15–25 %.

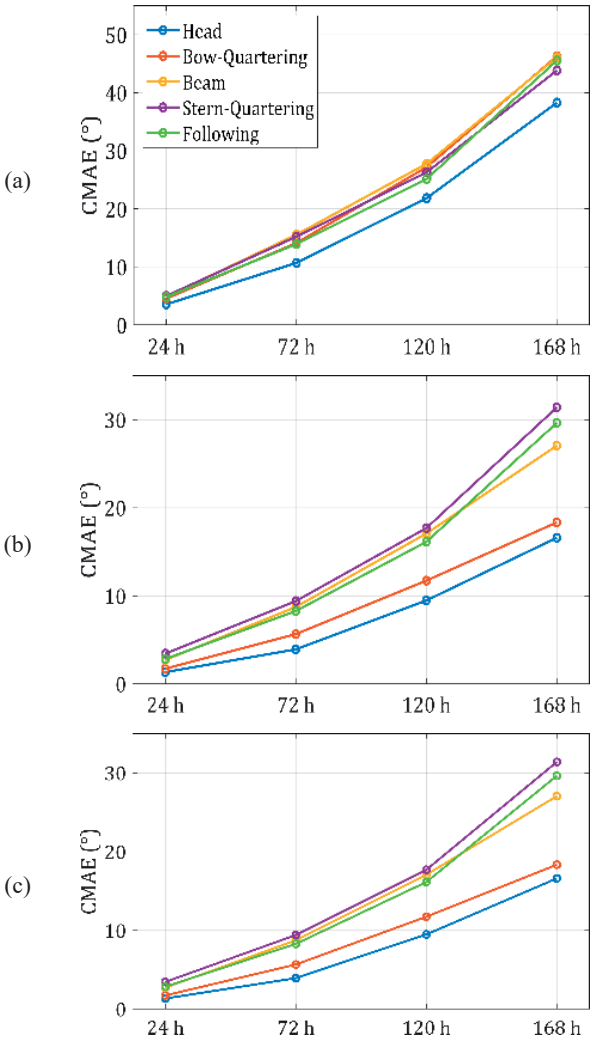

Fig. 1. Uncertainty measures for directional meteorological predictors in sea state WMO five, corresponding to significant wave heights between two point five and four metres: wind direction (*a*), wave direction (*b*), and encounter wave angle (*c*).

Uncertainty propagation to attainable ship speed varies across modelling approaches and operational conditions. For an intended speed of 14.5 kn in moderate seas, the JONSWAP-based NTPRO model exhibits RMSE growth from approximately 0.06–0.11 kn at 24 h to about 0.45–0.82 kn at 168 h, following an almost linear trend with acceleration beyond 72 h. MAE remains around 20 % lower, indicating the influence of occasional large deviations, while bias remains close to zero and agreement indices indicate stable performance.

The Pierson–Moskowitz implementation yields slightly higher uncertainty, with RMSE approaching 0.93 kn at maximum lead time, reflecting increased sensitivity to wave-field variability. Its spatial skill degrades more rapidly, and probabilistic calibration weakens beyond the medium range. NavCad produces the lowest overall uncertainty, with RMSE reaching roughly 0.76 kn at 168 h. Its stepped growth pattern reflects the quasi-static nature of the resistance model, while a small positive bias of about 0.25 kn indicates a tendency to overestimate speed loss. The relatively constant uncertainty growth rate of approximately 2% per hour suggests predictable behaviour, which is advantageous for risk-aware routing.

Correlation analysis was performed across all simulation cases to quantify how meteorological forecast errors propagate into attainable ship speed uncertainty. Pearson coefficients were computed between corresponding uncertainty metrics of predictor and response variables for 3 modelling approaches (NTPRO–JONSWAP, NTPRO–PM, NavCad), 2 reference speeds (12.0 and 14.5 kn), sea states 0–7, and 5 encounter-angle groups.

Three robust patterns emerge. First, a clear hierarchy governs uncertainty transfer: wave height shows the strongest and most consistent correlations with speed errors (typically 0.65–0.97 for RMSE and MAE), followed by wave period (0.45–0.85), while wind-related variables exhibit the widest variability (0.26–0.99). This reflects the dominant role of wave-induced resistance in speed loss. Second, the strength of the correlation depends strongly on the encounter geometry. Head seas (0–30°) yield the highest positive correlations, beam seas (75–105°) the weakest and most scattered, and following seas (150–180°) exhibit bimodal behaviour with either strong positive or negative coupling, indicating threshold effects in stern-wave interactions. Third, coupling intensifies with lead time: short-range forecasts (0–24 h) show moderate correlations (0.65–0.85), whereas long-range horizons (120–168 h) produce either very strong (>0.95) or very weak (<0.30) relationships, revealing increasing determinism or complete decoupling as forecast skill degrades.

For the 14.5 kn case under the Pierson–Moskowitz model, wave-height RMSE and MAE correlations remain consistently high (0.223–0.973), peaking in head seas (0.870–0.970) and increasing with lead time. Bias correlations are strongly negative (−0.713 to −1.000), indicating that wave-height overprediction directly induces speed underprediction. Wind-speed correlations are weaker by 8–10 % (0.259–0.996) and show predominantly positive bias, implying that wind overprediction tends to coincide with speed overprediction and suggesting limitations in aerodynamic modelling.

The JONSWAP implementation produces more polarised behaviour, with frequent near-perfect correlations (±1.000) at extended lead times, indicating overly deterministic uncertainty transfer under fully developed sea assumptions. CRPS correlations are largely negative in the head and following seas (−0.949 to −0.134), implying that improved probabilistic wind forecasts may reduce speed prediction reliability under strongly nonlinear conditions. UGR correlations vary widely (−0.858 to 0.890), with the strongest positive coupling in stern-quartering seas and extreme negative values in bow-quartering seas at short horizons, highlighting the strong geometry dependence of predictability.

6. Discussion and Conclusions

This study demonstrates that weather forecast uncertainty propagates into attainable ship speed in a structured yet highly nonlinear manner. By organising forecast observation pairs within sea-state bins, the proposed framework aligns uncertainty quantification with the way vessels experience weather in practice, spatially along their routes rather than at fixed locations. This enables statistically robust, operationally meaningful error characterisation that is directly applicable to routing algorithms.

The results show that forecast degradation is strongly variable-dependent. Significant wave height exhibits near-linear error growth in moderate conditions and accelerated degradation in severe seas, whereas wave period remains comparatively stable and well-calibrated. Wind speed displays the highest relative uncertainty, with nonlinear dependence on sea state and pronounced errors in both very calm and extreme conditions. Directional variables reveal even more complex behaviour: wind direction uncertainty is highly sensitive to sea state and forecast horizon, whereas wave direction remains comparatively stable due to the coherence of swell systems. Encounter wave angle, synthesising meteorological and navigational uncertainty, exhibits strong asymmetry between head and following seas, with up to 40 % higher uncertainty in following conditions. This asymmetry has direct implications for routing, as small directional errors can shift a vessel from benign following seas into hazardous quartering regimes.

Propagation to attainable ship speed preserves and amplifies these structures. All models exhibit increasing speed uncertainty with lead time, but with distinct characteristics. The JONSWAP-based implementation shows quasi-linear growth with limited bias, the Pierson–Moskowitz implementation is more sensitive to spatial variability and degrades faster beyond the medium range, while NavCad produces lower absolute uncertainty but introduces a systematic tendency to overestimate speed loss. These differences highlight that uncertainty is not solely a property of the forecast, but also of the vessel response model through which it is filtered.

Several limitations should be acknowledged. The analysis is restricted to a single vessel type and operational speed range. Although the simulation matrix covers wave heights up to 12 m, the correlation analysis focuses on sea states 0-7, reflecting typical routing conditions rather than survival scenarios. Extreme environments, where vessels would normally reroute, are therefore underrepresented. Ocean currents were neglected, and the coupling between wind and wave errors is based on the characteristics of the GFS-based dataset and the North Atlantic region.

Future work should extend the framework to multiple ship types and loading conditions, incorporate ocean current fields and fuel consumption models, and evaluate ocean

area-specific behaviour across different forecast systems. Finally, embedding the proposed uncertainty models into real-time optimisation algorithms will allow systematic assessment of risk-aware routing strategies in operational environments.

This work reframes weather routing from a deterministic optimisation problem into an uncertainty-aware decision process. Coupling meteorological predictability with vessel response provides a physically grounded basis for risk-informed navigation, where efficiency and reliability are treated as inseparable objectives.

Acknowledgement. This work has been supported by the Croatian Science Foundation under the project HRZZ-IP-2022-10-2821.

7. References

[1] Kim, M., Hizir, O., Turan, O., Day, S., Incecik, A., 2017. Estimation of added resistance and ship speed loss in a seaway. Ocean Engineering, 141, 465-476.

[2] Lang, X., Mao, W., 2020. A semi-empirical model for ship speed loss prediction at head sea and its validation by full-scale measurements. Ocean Engineering, 209, 107494.

[3] Vitali, N., Prpić-Oršić, J., Guedes Soares, C., 2020. Coupling voyage and weather data to estimate speed loss of container ships in realistic conditions. Ocean Engineering, 210, 106758.

[4] Jiao, J., Sun, S., Ren, H., 2016. Predictions of wave induced ship motions and loads by large-scale model measurement at sea and numerical analysis. Brodogradnja, 67(2), 81-100.

[5] Marjanović, M., Prpić-Oršić, J., Turk, A., Valčić, M., 2025. Anomalous Behavior in Weather Forecast Uncertainty: Implications for Ship Weather Routing. Journal of Marine Science and Engineering, 13(6), 1185.

[6] Ding, J.-F., Tseng, W.-J., Sung, Y.-J., 2024. An evaluation of operational risks for general cargo ship operators. Brodogradnja, 75(1), 75101.

[7] Valčić, M., Antonić, R., Tomas, V., 2011. ANFIS Based Model for Ship Speed Prediction. Brodogradnja, 62(4), 373-382.

[8] Moreira, L., Vettor, R., Guedes Soares, C., 2021. Neural net-work approach for predicting ship speed and fuel consumption. Journal of Marine Science and Engineering, 9(2), 119.

[9] Lu, D., Wang, A., Gan, H., Su, Y., Ao, X., 2025. A multi-objective collaborative optimization method of ship energy efficiency based on NSGA-II and TOPSIS. Brodogradnja, 76(3), 76301.

[10] Shin, G.-H., Yang, H., 2025. Deep reinforcement learning for integrated vessel path planning with safe anchorage allocation. Brodogradnja, 76(3), 76305.

[11] Guan, W., Xi, Z., Cui, Z., Zhang, X., 2025. Adaptive trajectory controller design for unmanned surface vehicles based on SAC-PID. Brodogradnja, 76(2), 76206.

[12] Ksciuk, J., Kuhlemann, S., Tierney, K., Koberstein, A., 2023. Uncertainty in maritime ship routing and scheduling: A literature review. European Journal of Operational Research, 308(2), 499-524.

[13] Vettor, R., Bergamini, F., Guedes Soares, C., 2021. A comprehensive approach to account for weather uncertainties in ship route optimization. Journal of Marine Science and Engineering, 9(12), 1434.

[14] Vettor, R., Guedes Soares, C., 2022. Reflecting the uncertainties of ensemble weather forecasts on the predictions of ship fuel consumption. Ocean Engineering, 250, 111009.

[15] Gao, J., Zhang, Y., 2024. Ship collision avoidance decision-making research in coastal waters considering uncertainty of target ships. Brodogradnja, 75(2), 75203.

[16] Wärtsilä, 2011. Wärtsilä Navigation simulator NTPRO 5000. Ship Speed Modeling in Wärtsilä NTPRO 5000.

[17] Zhang, S., Cheng, H., Deng, Z., Mei, L., Ding, L., Guo, C., Wang, X., Zhao, G., 2023. Navigational Safety Assessment of Ten-Thousand-Ton Vessels in Ship Tunnels by Ship Simulations. Water, 15(20), 3584.

[18] Fossen, T.I., 2011. Handbook of Marine Craft Hydrodynamics and Motion Control. John Wiley & Sons, Ltd., Hoboken, USA.

[19] HydroComp, 2023. NavCad - The premier hydrodynamic and propulsion system simulation software. https://www.hydrocompinc.com/solutions/navcad/

[20] HydroComp, 2024. HydroComp NavCad 2024 User's Guide. HydroComp, Inc.

[21] Bassam, A.M., Phillips, A.B., Turnock, S.R., Wilson, P.A., 2015. Ship voyage energy efficiency assessment using ship simulators. VI International Conference on Computational Methods in Marine Engineering (MARINE 2015), Rome, Italy, 15-17 June 2015.

[22] Yan, D., Chen, C., Gan, W., Sasa, K., He, G., Yu, H., 2025. Carbon intensity indicator (CII) compliance: Applications of ship speed optimization on each level using measurement data. Marine Pollution Bulletin, 212, 117593.

[23] Marjanović, M., Valčić, M., Prpić-Oršić, J., Barić, M., 2026. A data-driven framework for attainable ship speed uncertainty under stochastic weather conditions. Brodogradnja, 77(1), 77108.

[24] Buizza, R., Leutbecher, M., 2015. The forecast skill horizon. *Quarterly Journal of the Royal Meteorological Society*, 141, 3366-3382.

[25] Wilks, D.S., 2019. *Statistical Methods in the Atmospheric Sciences*, 4th ed. Academic Press, Cambridge, MA, USA.

[26] Willmott, C.J., Robeson, S.M., Matsuura, K., 2011. A refined index of model performance. *International Journal of Climatology*, 32(13), 2088-2094.

[27] Antonio, B., Aitchison, L., 2025. How to derive skill from the Fractions Skill Score. https://arxiv.org/abs/2311.11985 (accessed 5th July 2025)

[28] Hersbach, H., 2000. Decomposition of the continuous ranked probability score for ensemble prediction systems. *Weather and Forecasting*, 15, 559-570.

[29] Gneiting, T., Balabdaoui, F., Raftery, A.E., 2007. Probabilistic Forecasts, Calibration and Sharpness. *Journal of the Royal Statistical Society Series B: Statistical Methodology*, 69, 243-268.

[30] Rodwell, M.J., Wernli, H., 2023. Uncertainty growth and forecast reliability during extratropical cyclogenesis. *Weather and Climate Dynamics*, 4(3), 591-615.

Martina Bašić, Boris Ljubenkov, Ines Bezić*

Non-Newtonian fluid mechanics in engineering: A critical cross-sector review from process industries to marine technology

University of Split, Faculty of Electrical Engineering, Mechanical Engineering and Naval Architecture, Ruđera Boškovića 32, Split, 21000, Croatia
*Corresponding author: Martina.Basic.00@fesb.hr

Review article
Received: January 27, 2026
Accepted: April 214 2026
https://doi.org/10.65776/ep.20.4.5

Abstract

This review critically examines the role of non-Newtonian fluid mechanics across engineering systems, with particular emphasis on how knowledge developed in process industries can be applied and re-evaluated in marine technology. The paper first outlines the rheological framework commonly used to describe non-Newtonian behavior, including shear-dependent, yield-stress, viscoelastic, and thixotropic constitutive models, together with key dimensionless groups relevant to engineering interpretation: the Reynolds number in its generalized form, the Bingham number, the Deborah number, and the Weissenberg number. It then reviews representative engineering applications in process transport, drilling fluids, nanofluids, and additive manufacturing, not as isolated examples but as sources of cross-sector lessons for marine systems.

Special attention is given to maritime applications, including polymer-based drag reduction, brash-ice interaction, dredging slurries, heavy fuel oil handling, lubrication, firefighting foams, and adaptive damping systems. The review addresses bottlenecks in experimental characterization, computational modeling, and scale-up, with acknowledgment of where current models become uncertain or application-dependent. The available evidence suggests that the principal engineering value of non-Newtonian fluids lies in functions such as drag reduction, suspension stability, restart-pressure control, damping, and flow assurance; however, these benefits depend strongly on constitutive-model selection, parameter definition, formulation, and operating conditions. By integrating fundamental rheology with application-oriented comparison, this paper aims to provide a practically useful synthesis for engineers working at the interface of process and marine systems.

***Keywords**: non-Newtonian fluids; rheology; marine engineering; process engineering; drag reduction; ice-ship interaction; drilling fluids; nanofluids; viscoelasticity; thixotropy; CFD; EFD*

1. Introduction

In classical fluid dynamics, the assumption of constant viscosity greatly simplifies flow analysis. This Newtonian approximation is appropriate for water, air, and many low-molecular-weight liquids, and it remains the foundation of a large portion of conventional engineering design. In many industrial and natural systems, however, the relationship between stress and strain rate is not linear, and the apparent viscosity may depend on shear rate, time, temperature, field intensity, or deformation history. These materials are broadly classified as non-Newtonian fluids [1].

Such behavior is far from exceptional in engineering practice. Polymer melts, food pastes, slurries, drilling muds, greases, printing inks, foams, and field-responsive suspensions all exhibit rheological features that cannot be captured by a single constant viscosity [2-5]. In these systems, rheology is not merely an academic material property; it directly governs pressure drop, mixing efficiency, cuttings transport, restart pressure, heat-transfer performance, structural fidelity in deposition-based manufacturing, and energy consumption. Neglecting non-Newtonian behavior in design can therefore lead to pump under sizing, blockage events, unstable deposits, or unexpectedly high energy penalties.

The same point applies in marine engineering. External applications such as polymer drag reduction, brash-ice resistance, and dredging slurry transport involve fluids or fluid-like media whose resistance depends strongly on shear and yield behavior [9-13]. Internal ship systems also rely on rheologically complex materials, including heavy fuel oils, lubricants, firefighting foams, and magnetorheological suspensions [18-21]. The central challenge is therefore not simply to recognize that non-Newtonian fluids exist, but to identify which rheological feature governs a given engineering function, to select a constitutive model that faithfully represents that feature, and to validate predictions at operational scale.

1.1 Scope and Rationale

This review examines non-Newtonian fluid mechanics across a broad range of engineering applications, with a cross-sector structure that connects process industry paradigms to marine technology challenges. It combines cross-sector breadth with a unifying engineering question: how specific rheological features translate into practical design consequences.

The rationale for combining process industries with marine technology is that both domains confront closely re-

lated rheology-driven problems: pressure-drop prediction in shear-thinning transport, mobilization of yield-stress materials after stoppage, thixotropic structural recovery during intermittent operation, turbulence modification by viscoelastic additives, and the persistent difficulty of extrapolating laboratory rheology to full-scale systems. Process engineering offers mature paradigms and well-studied analogues for these issues, while marine engineering provides a demanding application environment in which the same constitutive ideas must operate under motion, scale effects, environmental constraints, and safety-critical conditions. Where these parallels are imperfect, or where the marine problem introduces genuinely distinct physics, those differences are noted explicitly.

1.2 Review Methodology

The literature for this review was assembled through a targeted survey of Scopus, Web of Science, and Google Scholar, supplemented by standard rheology texts and widely cited engineering references. Searches combined general keywords such as non-Newtonian fluids, rheology, and constitutive model with application-specific terms including drag reduction, brash ice, dredging slurry, heavy fuel oil, drilling mud, nanofluid, direct ink writing, magnetorheological fluid, CFD validation, and scale-up. Preference was given to foundational sources, widely cited review articles, and application papers that linked rheological behavior to identifiable engineering consequences.

The final selection is intended to be representative rather than exhaustive. In choosing references, priority was given to sources that clearly describe constitutive-model choice, discuss engineering implications, or identify important limitations in scaling, validation, or applicability. Where the literature in a sub-area remains sparse, that limitation is stated directly rather than masked by weakly related citations.

1.3 Specific Objectives and Paper Organization

The specific objectives of this review are:

To outline commonly used constitutive models for the principal classes of non-Newtonian behavior, including thixotropic and viscoelastic descriptions, together with the dimensionless groups commonly used in engineering interpretation.

To critically review representative applications in process and energy engineering, with emphasis on measurable engineering impacts, constitutive-model selection, and model limitations.

To examine marine applications in which non-Newtonian behavior materially affects vessel performance, onboard systems, or operational safety.

To identify recurring engineering bottlenecks - restart, scaling, validation, sustainability - and to connect them explicitly to constitutive behavior and model uncertainty.

The paper is organized as follows. Section 2 presents the rheological framework and defines the constitutive models and dimensionless groups used in engineering analysis. Section 3 reviews applications in mechanical and process engineering and extracts the lessons most relevant to marine systems. Section 4 examines applications in shipbuilding and marine technology. Section 5 discusses overarching challenges in validation, scaling, and implementation. Section 6 provides concluding remarks based on the literature reviewed here.

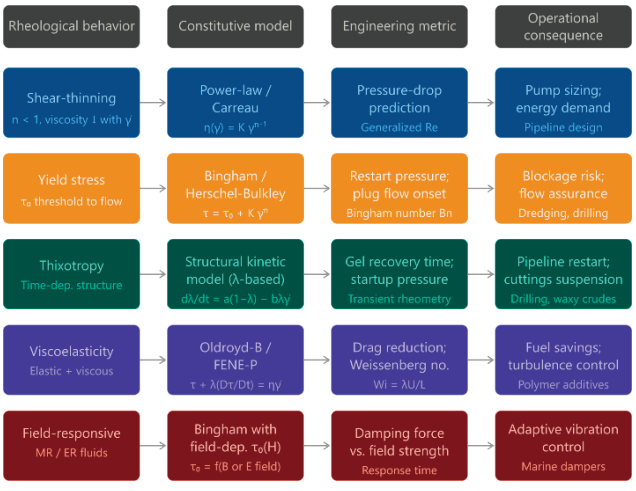

Figure 1 Rheology-to-design-consequence framework adopted in this review. Each row maps a dominant non-Newtonian behavior to its representative constitutive model, the engineering metric it governs, and the resulting operational consequence. Rows correspond to the five behavior classes examined in the paper: shear-thinning, yield stress, thixotropy, viscoelasticity, and field-responsive behavior.

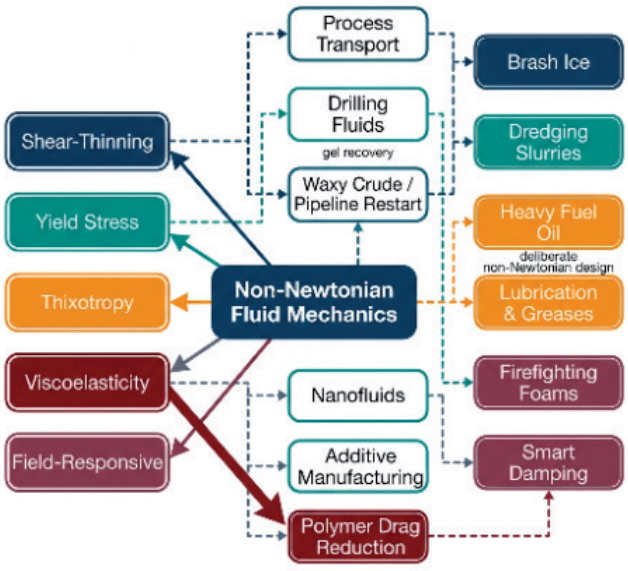

Figure 2 Engineering roles of non-Newtonian fluids across process and marine systems. The conceptual map links dominant rheological features – shear-thinning, yield stress, thixotropy, viscoelasticity, and field-responsive behavior – to major application clusters in both process and marine engineering domains.

2. Rheological Framework and Mathematical Formulation

2.1 Governing Equations

The motion of an incompressible non-Newtonian fluid is governed by conservation of mass and linear momentum. The momentum equation may be written as [3]:

$$\rho(Du/Dt) = -\nabla p + \nabla \cdot \tau + \rho g \qquad \text{(Eq. 1)}$$

where ρ is the density [kg m^{-3}], u is the velocity vector [m s^{-1}], p is the pressure [Pa], $\boldsymbol{\tau}$ is the extra-stress tensor [Pa], and g is the gravitational acceleration [m s^{-2}]. The distinction between Newtonian and non-Newtonian behavior lies in the constitutive relation defining $\boldsymbol{\tau}$. For generalized Newtonian descriptions, the apparent viscosity η depends on the scalar shear rate $\dot{\gamma}$ [s^{-1}], the magnitude of the rate-of-strain tensor. The engineering task is to select a constitutive model whose parameters are consistent with the stress range, time scale, and operating temperature of the application [4].

2.2 Time-Independent Constitutive Models

2.2.1 Power-Law (Ostwald-de Waele) Model

This law can be modelled as:

$$\tau = K\dot{\gamma}^{n} \qquad \text{(Eq. 2)}$$

where K is the consistency index [Pa s^n] and n is the flow behavior index [−]. When n < 1 the fluid is shear-thinning, when n > 1 it is shear-thickening. The model is analytically convenient but diverges at zero shear rate and does not capture viscosity plateaus; it is therefore a local approximation over a limited shear-rate window [4]. Representative values include drilling muds with K = 0.3–1.5 Pa s^n and n = 0.4–0.7, and dilute polymer solutions with n = 0.7–0.9.

2.2.2 Bingham Plastic Model

Bingham model can be written as:

$$\tau = \tau^0 + \mu_p\dot{\gamma}(\tau > \tau^0); \dot{\gamma} = 0(\tau \leq \tau^0) \qquad \text{(Eq. 3,4)}$$

where τ_0 is the yield stress [Pa] and μ_p is the plastic viscosity [Pa s]. The model is widely used for drilling fluids, greases, and idealized slurries; its engineering value lies in restart and mobilization analysis. The Bingham number $Bn = \tau_0 L / (\mu_p U)$, where L is a characteristic length [m] and U is a characteristic velocity [m s^{-1}], characterizes the relative importance of yield stress to viscous stress. When Bn >> 1, plug flow and blockage risk become more important; when Bn ≈ O(1), yield and viscous effects interact nonlinearly [4]. A practical limitation is that the model may underpredict startup demands for gelled materials with significant elastic storage.

2.2.3 Herschel-Bulkley Model

This model can be modelled as:

$$\tau = \tau^0 + K\dot{\gamma}^{n}(\tau > \tau^0) \qquad \text{(Eq. 5)}$$

The Herschel-Bulkley model combines finite yield stress with non-linear post-yield behavior, making it more physically realistic than the Bingham model for concentrated slurries, dredging mixtures, brash-ice analogues, and many drilling muds [5, 12, 13]. Typical parameter ranges reported for dredging-type slurries include τ_0 = 5–50 Pa, K = 0.05–0.5 Pa s^n, and n = 0.4–0.7.

2.3 Shear-Thinning Models with Finite Viscosity Plateaus

2.3.1 Cross and Carreau Models

When a wider shear-rate range must be represented, models with explicit low-shear (η_0) and high-shear (η_∞) viscosity plateaus are preferred. The Cross model:

$$\eta(\dot{\gamma}) = \eta\infty + (\eta^0 - \eta\infty)/[1 + (m\dot{\gamma})^{p}] \qquad \text{(Eq. 6)}$$

and the Carreau model:

$$\eta(\dot{\gamma}) = \eta\infty + (\eta^0 - \eta\infty)[1 + (\lambda\dot{\gamma})^2]^{-((1-n)/2)} \qquad \text{(Eq. 7)}$$

where λ is a characteristic relaxation time [s]. The Carreau model is numerically well-conditioned and preferred in CFD implementations where the power-law singularity at zero shear rate creates convergence problems. These models are appropriate for concentrated suspensions, foams, and lubricants whose apparent viscosity spans several orders of magnitude [4]. The comparison of the above-defined models is also visually explained by Figure 3.

2.4 Thixotropic Constitutive Models

Many engineering fluids - drilling muds, waxy crudes, firefighting foams - exhibit time-dependent structural recovery following shear. Simple steady-state viscosity functions are therefore insufficient to capture behavior during startup, stoppage, or intermittent operation. Thixotropy is represented by coupling a viscosity or stress equation to an internal structural variable λ (distinct from the relaxation time in Eq. 7), which evolves according to a kinetic equation [3, 28]:

$$d\lambda/dt = a(1 - \lambda) - b\lambda\dot{\gamma}^{\gamma} \qquad \text{(Eq. 8)}$$

where a and b are build-up and break-down rate constants and m is a fitting exponent. The apparent viscosity then depends on both $\dot{\gamma}$ and the instantaneous structural state λ. Elastoviscoplastic formulations extend this framework by including elastic stress storage in the gel network, which

can dominate restart behavior in waxy crudes and concentrated muds where purely viscoplastic Bingham estimates may underpredict the required restart pressure [28]. These models require transient rheometry for calibration but provide a more physically consistent basis for predicting startup pressure after extended shutdown.

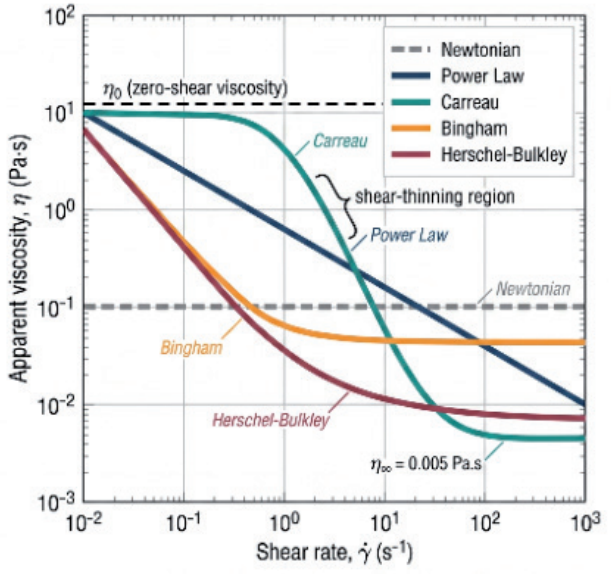

Figure 3 Apparent viscosity as a function of shear rate for key non-Newtonian constitutive models. Curves illustrate the characteristic responses of shear-thinning (power-law, Carreau), shear-thickening, Bingham plastic, and Herschel-Bulkley fluids, highlighting the divergence from Newtonian (constant viscosity) behavior across the shear-rate range.

2.5 Viscoelastic Constitutive Models

Polymer solutions used for drag reduction and smart-fluid systems exhibit memory effects and elastic stress storage that generalized Newtonian models cannot capture. The simplest linear viscoelastic description is the Maxwell model:

$$\tau + \lambda \partial\tau/\partial t = \eta\dot{\gamma} \qquad \text{(Eq. 9)}$$

The Maxwell model is, however, inadequate for strongly non-linear or turbulent flows. The Oldroyd-B model extends Maxwell to include a Newtonian solvent contribution and provides the simplest frame-indifferent viscoelastic model suitable for dilute polymer solutions. The Giesekus model introduces anisotropic drag through a mobility parameter α,

bringing predicted shear-thinning and extensional behavior closer to experimental data for concentrated polymer solutions used in drag reduction [3]. The FENE-P (Finitely Extensible Nonlinear Elastic - Peterlin) model accounts for finite chain extensibility and is particularly relevant to polymer degradation modeling, capturing the saturation of drag reduction at the maximum drag reduction (MDR) asymptote defined by Virk [11].

Two dimensionless groups are essential for characterizing viscoelastic effects. The Deborah number De = λ / t, where t is a characteristic flow time scale, quantifies elastic relaxation relative to flow kinematics: De << 1 implies quasi-viscous behavior; De >> 1 implies elastic-dominated response. The Weissenberg number Wi = λ $\dot{\gamma}$ characterizes the degree of polymer stretch in shear flow. In turbulent drag-reduction applications, onset and MDR regimes are well correlated with Wi, and any constitutive model intended for turbulence-closure coupling must reproduce the correct Wi dependence of the polymer stress [10, 11].

2.6 Field-Responsive (Magnetorheological and Electrorheological) Fluids

Magnetorheological (MR) and electrorheological (ER) fluids are suspensions in which an applied magnetic or electric field induces rapid particle alignment, producing a reversible and field-controllable increase in yield stress. Their behavior under an applied field is most accurately described by a modified Bingham model with a field-dependent yield stress:

$$\tau = \tau^0(H) + \mu_p\dot{\gamma} \qquad \text{(Eq. 10)}$$

where H is the applied magnetic field strength and $\tau_0(H)$ is an empirically determined function, typically approximated by $\tau_0 = c\,H^\alpha$ over a practical range [21]. Off-field, MR fluids are approximately Newtonian or weakly shear-thinning. The pre-yield elastic behavior can also be relevant in oscillatory damping applications, where the storage modulus G' contributes to the stiffness component of the damping force. It is important to note that the Maxwell-type scalar viscoelastic model (Eq. 9) does not provide a mechanistically adequate description of MR/ER behavior; these fluids require the field-dependent Bingham framework of Eq. 10 and its experimental calibration.

2.7 Engineering Interpretation of Constitutive-Model Selection

Model selection is not a purely mathematical exercise. It determines which engineering quantity can be predicted with reasonable confidence and at what computational cost. The power-law model may suffice for pressure-drop estimation over a limited shear-rate range. Restart analysis for gelled oils or drilling muds requires explicit yield-stress treatment and ideally thixotropic kinetics. Drag reduction and oscillatory damping cannot be understood without a viscoelastic or field-responsive framework. Turbulence-closure coupling requires models that correctly reproduce the Weissenberg-number dependence of polymer stress. Table 1 provides a consolidated summary.

Model	Governing Relation	Key Parameters	Dim. Group	Applications
Power-law	$\tau = K\dot{\gamma}^n$	K, n	Gen. Re	Polymer melts, slurries, inks
Bingham plastic	$\tau = \tau_0 + \mu_p\dot{\gamma}$	τ_0, μ_p	Bn	Drilling muds, greases
Herschel-Bulkley	$\tau = \tau_0 + K\dot{\gamma}^n$	τ_0, K, n	Bn, Gen. Re	Slurries, dredging, brash ice
Cross / Carreau	See Eqs. 6-7	η_0, η_∞, λ, n	Ca	Lubricants, foams, CFD
Thixotropic EVP	Eq. 7 + kinetics (Eq. 8)	a, b, m, moduli	Bn + De	Waxy crudes, gelled muds
Maxwell / Oldroyd-B	$\tau + \lambda D\tau/Dt = ...$	η_s, η_p, λ	De, Wi	Polymer drag reduction
Giesekus / FENE-P	See ref. [3]	α or b, λ	Wi	Turbulent drag reduction
MR/ER Bingham	$\tau = \tau_0(H) + \mu_p\dot{\gamma}$	$\tau_0(H)$, c, α	Mn	Adaptive dampers

Table 1. Summary of principal constitutive models for engineering non-Newtonian fluids

3. Applications in Mechanical and Process Engineering

Process-industry applications provide controlled, well-studied examples of the same rheology-driven phenomena that appear in marine technology. In each case, the key questions are: which constitutive feature governs engineering performance, how large is the engineering consequence of getting it wrong, and where do current models break down?

3.1 Fluids in the Chemical and Process Industries

In process engineering, the fluid is often the product, and its rheology governs transport, mixing, and handling. Polymer melts, food pastes, personal-care formulations, and slurries frequently display strong shear dependence, making pressure-drop prediction and pump selection more complex than in Newtonian transport [2, 4]. In practical terms, the use of generalized Reynolds number analysis can materially change flow-regime interpretation and therefore affect pump selection and flow-stability assessment. For example, a power-law fluid with $n = 0.5$ can yield a generalized Reynolds number two to three times lower than the Newtonian estimate at the same bulk velocity, shifting the predicted flow regime from turbulent to transitional.

The same fluid may exhibit high apparent viscosity during storage or startup, substantially increasing restart loads and promoting maldistribution in pipes or manifolds. This tension between low-shear and high-shear behavior - which neither the power-law nor a single-point viscosity measurement can resolve - is the reason that multi-parameter models with explicit viscosity plateaus are preferred for serious design work.

3.2 Non-Newtonian Fluids in the Energy Sector

Drilling Muds

Drilling fluids are classic engineered non-Newtonian systems because they must satisfy contradictory requirements: shear-thin during circulation to limit frictional pressure losses yet recover structure rapidly during stoppage to suspend drill cuttings and maintain borehole stability [5]. The engineering consequence of thixotropy is specific: cuttings suspension during stoppage depends on whether the yield stress builds

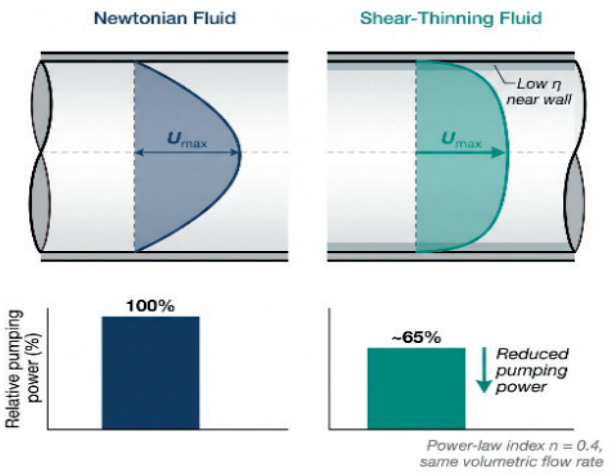

Figure 4 Velocity profiles in fully developed pipeline flow for Newtonian and shear-thinning fluids. Decreasing the power-law index n progressively flattens the profile toward plug-like flow, with significant implications for pressure-drop estimation and mixing efficiency in industrial pipe systems.

back to a value exceeding the critical threshold $\tau_0 > \rho_p\, d_p\, g / 6$ (for spherical particles of diameter d_p and density ρ_p) within the available time window. Recent studies show that nanoparticle additives can modify yield point, gel strength, and apparent viscosity [26, 27], but the direction and magnitude of the effect remain formulation-dependent - a recurring pattern in non-Newtonian engineering.

Waxy Crude Oils

Waxy crude oil transport provides an especially clear example of rheology producing a measurable design constraint. When oil cools below the wax appearance temperature, crystallized wax forms a gel network and the

material develops an apparent yield stress [6]. The principal engineering consequence is restart pressure after shutdown, which can dominate pipeline and pumping-system design. Recent elastoviscoplastic thixotropic formulations - validated against transient restart experiments - demonstrate that Bingham-type estimates can underpredict restart pressure by factors of 1.5 to 3 when elastic energy stored in the gel network contributes significantly to the initial mobilization force [28]. This discrepancy directly determines whether an installed pump has adequate startup capacity.

3.3 Nanofluids and Heat Transfer

Nanofluids are often cited as heat-transfer enhancers because dispersed nanoparticles can increase effective thermal conductivity. The critical engineering question, however, is whether the thermal benefit outweighs the hydraulic penalty, particularly when the suspension becomes non-Newtonian at practically relevant concentrations [7, 29, 30]. Recent systematic reviews indicate that Al_2O_3 nanofluids at volume fractions above 1-2% exhibit measurable increases in apparent viscosity at low shear rates, which can raise pumping power requirements by 10-30% depending on flow regime and system geometry [29, 30]. Engineering assessment must therefore use a figure of merit that integrates Nusselt number gain against pressure-drop penalty over the full operating range.

3.4 Rheology in Advanced Manufacturing

Direct ink writing and related extrusion-based additive manufacturing processes depend critically on non-Newtonian behavior [8, 31]. The ink must shear-thin sufficiently to flow through a nozzle at moderate pressure, yet recover yield stress rapidly enough after deposition to maintain structural fidelity. The time scale of structural rebuilding - quantified by the thixotropic recovery half-time - is as important as the steady-state constitutive curve. The engineering criterion is therefore a specific ratio of deposition time to recovery time, which must be matched to the constitutive model calibrated at the relevant shear rates (typically 10^2-10^4 s^{-1} at the nozzle wall).

3.5 Cross-Sector Lessons and Engineering Bottlenecks

Across the process applications reviewed above, the same engineering bottlenecks recur:

1. Pressure-drop prediction in fluids whose apparent viscosity changes strongly with shear rate, requiring generalized Reynolds number analysis and model-specific friction-factor correlations.
2. Restart and mobilization of materials that develop yield stress or elastic structure during stoppage, where Bingham models are insufficient and elastoviscoplastic thixotropic formulations are required.
3. Time-dependent recovery in thixotropic systems, where constitutive parameters must be calibrated from transient rather than steady-state rheometry.
4. Trade-offs between single-metric performance enhancement and system-level efficiency, illustrated most clearly by nanofluids and polymer-additive systems.
5. Sensitivity of constitutive parameters to temperature, formulation, and scale, which limits the direct transferability of laboratory data to design calculations.

These bottlenecks provide the main conceptual bridge to marine technology. The marine problem is not fundamentally different in kind; it is different in consequence, scale, and environmental severity. Table 2 summarizes the comparison with explicit governing dimensionless groups.

Engineering Issue	Process Example	Marine Analogue	Governing Feature	Dim. Group	Consequence
Pressure-drop prediction	Polymer / slurry transport	Dredging; onboard piping	Shear-thinning viscosity	Gen. Re	Pump sizing; energy
Restart after stoppage	Waxy crude pipelines	Heavy fuel oil lines (viscosity-controlled)	Temp.-dependent viscosity; gel network in some grades	Bn; EVP model	Startup pressure; flow assurance
Suspension at rest	Drilling muds	Firefighting foams; sediment	Yield stress; rebuild rate	Bn; recovery time	Suspension; blockage prevention
Flowability vs. retention	Direct ink writing	Coatings and foams	Recovery kinetics; viscoelasticity	De; half-time	Coverage; structural persistence
Enhancement vs. penalty	Nanofluids	Cooling and lubrication	Viscosity-conductivity trade-off	Nu/Re ratio	Net system efficiency

Table 2. Cross-sector engineering bottlenecks linking process and marine applications

4. Applications in Shipbuilding and Marine Technology

The marine environment gives non-Newtonian fluid mechanics a distinct practical significance. Marine operations combine large scale, unsteady forcing, limited maintenance windows, severe environmental exposure, and tight safety margins. For this reason, marine applications are especially demanding tests of whether constitutive descriptions developed in laboratory or process-industry settings remain valid under operational conditions.

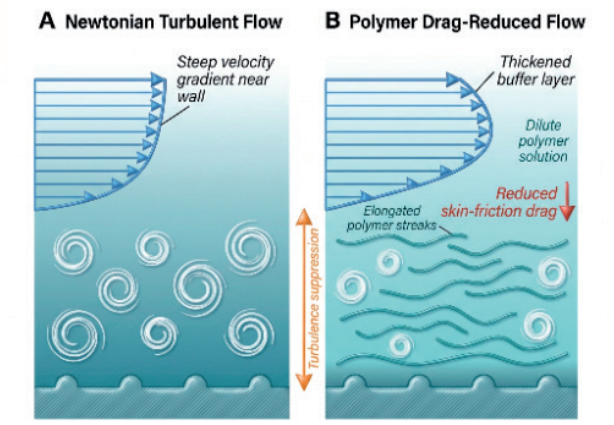

Figure 5 Comparison of velocity profiles in Newtonian turbulent pipe flow and polymer-induced drag-reduced flow at equivalent Reynolds number. The drag-reduced profile exhibits a thickened buffer layer and suppressed turbulent fluctuations, consistent with the Virk maximum drag reduction asymptote for dilute polymer solutions.

4.1 Frictional Drag Reduction

Polymer-based drag reduction is one of the most frequently cited maritime applications of non-Newtonian rheology. The fundamental mechanism involves viscoelastic polymer additives interacting with near-wall turbulent structures, suppressing quasi-streamwise vortices responsible for skin-friction drag [9-11]. The onset and intensity of drag reduction are well correlated with the Weissenberg number $Wi = \lambda U / \delta$, where δ is the viscous length scale. The maximum drag reduction (MDR) asymptote, as defined by Virk [11], sets an upper bound independent of polymer type above a threshold concentration and De.

The practical engineering consequence is measurable: under controlled conditions, drag reductions of 40-70% have been reported in pipe flow [10, 22, 23]. However, these laboratory values are not directly transferable to full-scale marine use for three reasons. First, polymer degradation under high shear rates progressively reduces molecular weight and viscoelastic relaxation time. Second, the interaction of polymer additives with turbulent boundary layers in the presence of surface roughness is not captured by smooth-wall correlations. Third, scale effects in the transition to full ship Reynolds numbers are not well quantified. The critical limitation remains predictability and durability at operational scale, not proof of concept.

4.2 Ice-Ship Interaction and Brash Ice

For vessels operating in polar and ice-obstructed waters, broken or crushed ice may behave as a dense fluid-like medium rather than as discrete rigid blocks. In such conditions, continuum constitutive models become applicable, and Bingham or Herschel-Bulkley formulations have been used to represent yield-stress behavior in brash ice [12]. The engineering quantity of direct interest is ice resistance, which determines propulsion demand, route planning, and ice-class design margins.

The constitutive-model choice is consequential. A Bingham approximation may overpredict resistance if the actual post-yield behavior is strongly shear-thinning. A Herschel-Bulkley formulation with $n < 1$ can produce resistance predictions that are 10-20% lower than Bingham estimates at high vessel speeds - a difference large enough to affect ice-class power requirements. The critical limitation is equally important: as floe size increases relative to hull dimensions, discrete-element or coupled continuum-discrete methods become necessary, and the Herschel-Bulkley model should not be applied beyond its range of validity.

4.3 Sediment Slurries and Dredging Operations

Dredging slurries are among the clearest marine examples of rheology-controlled transport. High-concentration water-sand-mud mixtures often exhibit both shear-thinning and yield-stress characteristics [13]. Their rheology affects pressure loss, critical deposition velocity, wear, and blockage risk in pipelines and pumping equipment. The engineering consequence of poor rheological characterization is immediate and measurable: underestimating yield stress can lead to undersized pumps and increased blockage probability, whereas overestimating it increases installed power and operating cost.

For practical dredging design, the critical deposition velocity - below which settled-bed formation and blockage become probable - depends on both particle size distribution and the yield stress of the slurry matrix. Herschel-Bulkley parameters must be validated for the specific solids loading and particle-size distribution of the actual material, because laboratory analogues may not reproduce the rheological behavior of in-situ marine sediments.

4.4 Onboard Fluid Management: From Fuel to Firefighting

Heavy Fuel Oil Handling

Heavy fuel oil (HFO) handling aboard ships presents an operationally demanding flow-assurance problem that is fundamentally different from the waxy-crude pipeline problem described in Section 3.2, and this distinction must be stated clearly. While waxy crudes develop a genuine yield-stress gel network upon cooling, HFO behavior in normal ship operation is primarily governed by temperature-dependent Newtonian or weakly non-Newtonian viscosity, managed through preheating, insulation, and fuel-treatment systems rather than detailed yield-stress

constitutive characterization [18]. The relevant engineering metrics are kinematic viscosity at the injection temperature (typically 10-15 cSt for adequate atomization), startup pumpability during cold conditions, and the viscosity-temperature sensitivity across the expected operating range.

In practice, this distinction matters for design: if HFO is treated as a Bingham or thixotropic material analogous to waxy crude, flow-assurance calculations may be misleadingly conservative in some respects. The correct engineering approach is to apply temperature-dependent viscosity correlations validated for the specific fuel grade, design heating systems for the full viscosity-temperature curve, and verify pump startup margins against the maximum expected viscosity at minimum service temperature. Where specific HFO grades exhibit non-Newtonian behavior under near-ambient conditions, this should be verified by dedicated rotational rheometry rather than assumed from analogy with waxy crudes.

Lubricants and Greases

Marine lubricants and greases exhibit non-Newtonian behavior by design. Shear-thinning allows a lubricant to flow effectively in high-shear contacts while maintaining sufficient apparent viscosity at lower shear rates to resist leakage and provide surface retention [19]. The engineering advantage is quantifiable in terms of load-support capacity, friction coefficient reduction, and lubricant retention time. The constitutive response must remain stable over temperature range and service duration; thermo-oxidative degradation that alters molecular-weight distribution can shift n and K systematically, leading to unexpected changes in film thickness and contact protection.

Firefighting Foams

Firefighting foams provide an example in which engineering function depends critically on a balance between easy pumping and post-deployment stability [20, 24]. A foam must shear-thin during pumping and nozzle flow, yet rebuild structural integrity after deployment to spread and persist over a fuel surface long enough to prevent reignition. The relevant rheological issues - shear-thinning during flow, structural recovery at rest - are physically analogous to those in direct ink writing and thixotropic recovery in drilling fluids. However, the time scales, temperature conditions, and contamination environment are specific to firefighting applications and cannot be assumed from generic aqueous-foam rheology studies [24]. Application-specific characterization under realistic conditions is required.

4.5 Smart Fluids in Damping and Control Systems

Magnetorheological and electrorheological fluids extend the discussion from passive to actively controlled rheological response. Under an applied field, the field-dependent yield stress increases rapidly (Section 2.6), allowing controllable and real-time-adjustable damping behavior [21]. Marine-engine isolation studies illustrate this potential: AI-assisted nonlinear controllers combined with MR dampers have demonstrated measurable reductions in low-frequency engine vibration transmitted to ship structure [25]. The engineering advantage is specific: the damping force can be tuned continuously to the excitation spectrum rather than fixed by passive hardware.

However, the limitations are substantial. The rheological behavior of MR fluids is described by a field-dependent Bingham model (Eq. 10), and the pre-yield elastic behavior also contributes to the stiffness component of the damping force in oscillatory applications; neglecting this contribution leads to systematic underprediction of peak force at small strains. Long-term stability (particle settling, carrier-fluid degradation), control-system reliability in marine environments, and power requirements for field generation are important barriers that remain incompletely resolved. The technology is best characterized as technically promising and demonstrably functional at laboratory scale, but still requiring substantive validation under full marine service conditions before widespread adoption.

Application	Dominant Rheology	Key Model	Engineering Metric	Main Benefit	Critical Limitation
Polymer drag reduction	Viscoelasticity	Oldroyd-B / Giesekus / FENE-P	Frictional resistance; fuel demand	40-70% drag reduction (lab)	Degradation; scale-up; roughness
Brash-ice interaction	Yield stress; shear-thinning	Bingham or Herschel-Bulkley	Ice resistance; propulsion power	More realistic prediction (~10-20% vs. Bingham)	Continuum validity; large-floe physics
Dredging slurries	Yield stress; shear-thinning	Herschel-Bulkley	Pressure drop; deposition velocity	Reliable pipeline transport design	Solids-content sensitivity; in-situ calibration
Heavy fuel oil handling	Temp.-dependent viscosity (Newtonian)	Viscosity-temperature correlation	Startup pumpability; atomization viscosity	Flow assurance via heating design	Sensitivity to fuel grade and temperature history
Firefighting foams	Shear-thinning; structural recovery	H-B + recovery kinetics	Pumpability; blanket persistence	Efficient delivery and surface coverage	Stability under fire; application-specific calibration
Smart damping (MR) fluids	Field-responsive yield stress + pre-yield elasticity	Bingham with $\tau_0(H)$	Damping force; response bandwidth	Adaptive vibration control	Particle settling; power; marine environment durability

Table 3. Comparative synthesis of selected marine non-Newtonian applications

5. Challenges and Future Directions

Although the application range reviewed above is broad, three recurring challenges limit the predictive reliability and operational deployment of non-Newtonian fluid mechanics in engineering.

5.1 Validation: Physical and Numerical

The first challenge is validation of constitutive models and their engineering predictions. Experimental fluid dynamics remains indispensable because rheological parameters measured under idealized laboratory conditions are often insufficient to characterize the complex thermal, compositional, and transient histories encountered in service. This is particularly true for thixotropic fluids, viscoelastic drag reducers, and opaque slurries, where reproducible measurements require careful instrument selection and conditioning protocols [13, 16].

Computational fluid dynamics provides a powerful complementary tool, but its predictive quality in non-Newtonian flows depends on both the constitutive model and the turbulence closure. Standard two-equation eddy-viscosity models (e.g., k-ω SST [15]) are calibrated for Newtonian turbulence; their extension to viscoelastic or yield-stress flows introduces additional sources of error because the constitutive model affects the effective viscosity distribution across the boundary layer, and the turbulence-constitutive coupling is not captured by modified eddy-viscosity approaches. Verification and validation protocols such as those outlined by Stern et al. [16] should be applied explicitly in any CFD study claiming to predict non-Newtonian engineering performance.

5.2 The Scaling Problem

Scale-up remains one of the most difficult issues in non-Newtonian engineering. Classical Froude and Reynolds similarity arguments assume invariant fluid properties, whereas non-Newtonian fluids exhibit apparent viscosity and relaxation behavior that depend on local shear rate, time scale, and temperature [14, 17]. A drag-reducing polymer that performs well in a small facility at $Wi \approx 10$ will experience a different Wi at ship scale - because the viscous length scale δ decreases with increasing Re - meaning the same polymer may produce a different drag-reduction level simply because of the scale change. Likewise, Herschel-Bulkley parameters determined in a laboratory slurry loop may not represent the in-situ behavior of a dredging slurry at full operational solids loading and pipe diameter.

Future progress requires combining targeted experiments at multiple scales, non-Newtonian similarity analyses that account for shear-rate-dependent viscosity in the scaling criteria, and high-quality CFD with constitutive models validated at intermediate scales before extrapolation to full scale.

5.3 Economic, Operational, and Environmental Constraints

Even when a rheological concept is physically sound, implementation may still be limited by cost, reliability, or regulation. Polymer drag reduction requires storage, injection infrastructure, and environmental acceptability under marine discharge regulations. Heavy fuel oil systems require dependable heating and monitoring infrastructure. MR damping systems require sensors, controllers, and functional stability of the MR fluid under continuous cyclic loading.

Environmental constraints are tightening. Marine applications that rely on chemical additives must be evaluated not only for performance but for discharge impact and regulatory compatibility under MARPOL and regional frameworks. This pressure is encouraging interest in lower-impact materials, closed-loop deployment systems, and application-specific justification rather than routine additive use.

5.4 Research Priorities

Based on the literature reviewed, the most productive research directions are:

27. Better integration of transient rheometry with engineering-scale validation, particularly for thixotropic and elastoviscoplastic systems where steady-state constitutive curves are insufficient.
28. Development and experimental validation of constitutive closures for turbulent flows of viscoelastic fluids, extending beyond Maxwell and Oldroyd-B to Giesekus and FENE-P models coupled with appropriate turbulence treatments.
29. Application-specific scaling strategies for marine drag reduction and onboard deployment systems, explicitly accounting for Wi-Re co-variation across scales.
30. Systematic comparison frameworks that connect rheological behavior directly to engineering metrics, parameter uncertainties, and operational risk.
31. Expanded marine-specific full-scale evidence for brash-ice constitutive behavior, HFO non-Newtonian rheology under realistic temperature histories, and MR damper performance under marine service conditions.

6. Conclusion

This review has examined non-Newtonian fluid mechanics across process and marine engineering with the objective of moving beyond descriptive survey toward a more structured, quantitatively grounded synthesis. The principal conclusion is that the engineering value of non-Newtonian fluid mechanics lies in its capacity to explain and exploit functions that Newtonian descriptions cannot represent adequately: shear-dependent pumpability, yield-stress mobilization, thixotropic rebuilding, viscoelastic drag reduction, and field-responsive damping. Each of these functions is associated with specific constitutive models and dimensionless groups, and the choice of model determines which engineering quantities can be predicted with defensible confidence.

Several evidence-based conclusions emerge from the analysis. First, quantitative engineering benefits must be

stated with explicit constitutive dependence. Polymer drag reduction can reduce frictional resistance by 40-70% under controlled conditions, but the scale-dependent Weissenberg number and polymer degradation constraints limit direct application of laboratory values to ship design. Herschel-Bulkley treatment of brash ice yields resistance predictions 10-20% below Bingham estimates at high vessel speeds, a difference with practical ice-class implications. Bingham-only restart models for gelled systems can underpredict the required restart pressure by factors of 1.5 to 3 when elastic network contributions are present.

Second, constitutive-model choice is not interchangeable. Power-law models are adequate for pressure-drop estimation over limited shear-rate ranges but fail at low shear rates and in startup analysis. Bingham models provide efficient yield-stress design tools but must be replaced by elastoviscoplastic thixotropic formulations wherever gel elasticity is significant. Maxwell-type viscoelastic models are useful conceptual tools but are insufficient for turbulence-closure coupling in drag-reduction CFD, where Giesekus or FENE-P models are required. MR/ER fluids require a field-dependent Bingham model rather than a scalar viscoelastic analogy. Heavy fuel oil handling is primarily a temperature-dependent Newtonian viscosity problem in normal ship operation and should be treated as such - not by analogy with yield-stress waxy crudes.

Third, the largest practical gap is often not conceptual but translational: laboratory constitutive characterization, numerical prediction with coupled turbulence-constitutive closures, and full-scale engineering validation remain imperfectly connected. The most important research investments are in transient rheometry for thixotropic and viscoelastic systems, non-Newtonian scaling strategies that account for shear-rate-dependent viscosity, and application-specific validation at intermediate and full scale. When non-Newtonian fluid mechanics is treated with that level of rigor, it provides a coherent and quantitatively useful design framework for both process and marine systems.

7. References

[1] W.-T. Wu and M. Massoudi, “Recent advances in mechanics of non-Newtonian fluids,” Fluids, vol. 5, no. 1, p. 10, 2020, doi: 10.3390/fluids5010010.

[2] G. R. Kasat and A. B. Pandit, “Review on mixing characteristics in solid-liquid and solid-liquid-gas reactor vessels,” Can. J. Chem. Eng., vol. 83, no. 4, pp. 618-643, 2005, doi: 10.1002/cjce.5450830407.

[3] R. B. Bird, R. C. Armstrong, and O. Hassager, Dynamics of Polymeric Liquids, Volume 1: Fluid Mechanics, 2nd ed. New York: Wiley, 1987.

[4] R. P. Chhabra and J. F. Richardson, Non-Newtonian Flow and Applied Rheology: Engineering Applications, 2nd ed. Oxford: Butterworth-Heinemann, 2011.

[5] R. Caenn, H. C. H. Darley, and G. R. Gray, Composition and Properties of Drilling and Completion Fluids, 6th ed. Oxford: Gulf Professional Publishing, 2011.

[6] L. T. Wardhaugh and D. V. Boger, “The flow characteristics of waxy crude oils,” Chem. Eng. Res. Des., vol. 69, no. A3, pp. 115-124, 1991, doi: 10.1016/0263-8762(91)80042-Z.

[7] J. Yang et al., “Review on thermal performance of nanofluids with and without magnetic fields,” Front. Energy Res., vol. 10, p. 822776, 2022, doi: 10.3389/fenrg.2022.822776.

[8] C. G. Compton and J. A. Lewis, “3D-printing of lightweight cellular composites,” Adv. Mater., vol. 26, no. 34, pp. 5930-5935, 2014, doi: 10.1002/adma.201401804.

[9] B. A. Toms, “Observation on the flow of linear polymer solutions through straight tubes at large Reynolds numbers,” in Proc. 1st Int. Congr. Rheology, vol. 2, Amsterdam: North-Holland, 1948, pp. 135-141.

[10] M. Perlin, D. R. Dowling, and S. L. Ceccio, “Freeman scholar review: The physics and mechanisms of drag reduction,” J. Fluids Eng., vol. 138, no. 9, p. 091208, 2016, doi: 10.1115/1.4033571.

[11] P. S. Virk, “Drag reduction fundamentals,” AIChE J., vol. 21, no. 4, pp. 625-656, 1975, doi: 10.1002/aic.690210402.

[12] A. Kulyakhtin, “Numerical modelling of ice channel properties,” Cold Regions Sci. Technol., vol. 65, no. 3, pp. 289-297, 2011, doi: 10.1016/j.coldregions.2010.10.006.

[13] N. Eshtiaghi et al., “Sludge rheology: A review of instrumentations and measurement strategies,” Rheol. Acta, vol. 52, pp. 1011-1049, 2013, doi: 10.1007/s00397-013-0732-4.

[14] ITTC, “Recommended Procedures and Guidelines: Resistance Test,” Procedure 7.5-02-02-01, 29th ITTC, 2021.

[15] F. R. Menter, “Two-equation eddy-viscosity turbulence models for engineering applications,” AIAA J., vol. 32, no. 8, pp. 1598-1605, 1994, doi: 10.2514/3.12149.

[16] F. Stern et al., “Comprehensive approach to verification and validation of CFD simulations,” J. Fluids Eng., vol. 123, no. 4, pp. 793-802, 2001, doi: 10.1115/1.1412235.

[17] P. S. Granville, The Frictional Resistance and Turbulent Boundary Layer of Rough Surfaces. Washington, DC: David Taylor Model Basin, 1958.

[18] H. D. McGeorge, Marine Auxiliary Machinery, 7th ed. Oxford: Butterworth-Heinemann, 1998.

[19] A. R. Lansdown, Lubrication and Lubricant Selection: A Practical Guide, 3rd ed. Bury St Edmunds: Professional Engineering Publishing, 2004.

[20] Y. Bao et al., “Experimental study on rheological behavior of firefighting foams,” Materials, vol. 18, no. 14, p. 3236, 2025, doi: 10.3390/ma18143236.

[21] M. R. Jolly, J. W. Bender, and J. D. Carlson, “Properties and applications of commercial magnetorheological fluids,” J. Intel. Mater. Syst. Struct., vol. 10, no. 1, pp. 5-13, 1999, doi: 10.1177/1045389X9901000102.

[22] W. A. Rowin et al., “A novel approach for drag reduction using polymer coating,” Ocean Eng., vol. 240, p. 109895, 2021, doi: 10.1016/j.oceaneng.2021.109895.

[23] J. D. Cussuol et al., “Polymer drag reduction regeneration,” J. Non-Newtonian Fluid Mech., vol. 321, p. 105126, 2023, doi: 10.1016/j.jnnfm.2023.105126.

[24] B. Dollet and C. Raufaste, “Rheology of aqueous foams,” Comptes Rendus Physique, vol. 15, no. 8-9, pp. 731-747, 2014, doi: 10.1016/j.crhy.2014.09.008.

[25] M. Yang et al., “Nonlinear controller supported by artificial intelligence of the rheological damper system,” J. Low Freq. Noise Vib. Active Control, vol. 42, no. 4, pp. 1919-1936, 2023, doi: 10.1177/14613484231187780.

[26] A. K. Abbas et al., “Improving hole cleaning in horizontal wells by using nanocomposite water-based mud,” J. Pet. Sci. Eng., vol. 203, p. 108619, 2021, doi: 10.1016/j.petrol.2021.108619.

[27] A. M. Alkalbani et al., “Insightful study on the effect of zinc oxide nanoparticle diameter on the rheology of water base mud,” J. Pet. Sci. Eng., vol. 217, p. 110878, 2022, doi: 10.1016/j.petrol.2022.110878.

[28] Y. Bao and J. Zhang, “Restart behavior of gelled waxy crude oil pipeline based on an elasto-viscoplastic thixotropic model,” J. Non-Newtonian Fluid Mech., vol. 284, p. 104377, 2020, doi: 10.1016/j.jnnfm.2020.104377.

[29] R. J. Issa, “A review on thermophysical properties and Nusselt number behaviour of Al2O3 nanofluids,” J. Therm. Sci., vol. 30, pp. 418-431, 2021, doi: 10.1007/s11630-021-1266-1.

[30] Y. Wang et al., “Evaluation methods of thermo-hydraulic performance in nanofluids,” Appl. Therm. Eng., vol. 240, p. 121989, 2024, doi: 10.1016/j.applthermaleng.2023.121989.

[31] M. A. S. R. Saadi et al., “Direct ink writing: A 3D printing technology for diverse materials,” Adv. Mater., vol. 34, no. 28, p. e2108855, 2022, doi: 10.1002/adma.202108855.

Engineering Power – *Bulletin of the Croatian Academy of Engineering*
Vol. 20(4) 2025 – ISSN 2718-322X (Online)
Publisher: Croatian Academy of Engineering (HATZ), 28 Kačić Street, P.O. Box 14, HR-10000 Zagreb, Republic of Croatia
Editor-in-Chief: Prof. Vedran Mornar, Ph.D., President of the Academy
University of Zagreb Faculty of Electrical Engineering and Computing
Editor: Prof. Bruno Zelić, Ph.D., Vice-President of the Academy
University of Zagreb Faculty of Chemical Engineering and Technology
Guest Editor: Prof. Nastia Degiuli, Ph.D., University of Zagreb Faculty of Mechanical Engineering and Naval Architecture
Activities Editor: Tanja Miškić Rogić
Editorial Board: Prof. Vedran Mornar, Ph.D., Prof. Vladimir Andročec, Ph.D., Prof. Bruno Zelić, Ph.D., Assoc. Prof. Mario Bačić, Ph.D., Prof. Neven Duić, Ph.D.
Editorial Board Address: Croatian Academy of Engineering (HATZ), "Engineering Power" – Bulletin of the Croatian Academy of Engineering, Editorial Board, 28 Kačić Street, P.O. Box 14, HR-10000 Zagreb, Republic of Croatia
E-mail: hatz@hatz.hr
Graphical and Technical Editor: Tiskara Zelina, Ltd., Zelina

The publication of the Engineering Power journal was financially supported by the Ministry of Science, Education and Youth within the project Strengthening publishing activities, cooperation with industry, and the national and international visibility of technical and biotechnical sciences through the programmes and activities of the Croatian Academy of Engineering, pursuant to the Financial Assistance Agreement dated May 20, 2026.